Available online at www.sciencedirect.com

ScienceDirect

Underground Space 25 (2025) 195–217

www.keaipublishing.com/undsp

Research Paper

Hydraulic-rock-structural responses of close-spaced shield-driven twin tunnels: Insights from in-situ monitoring and three-dimensional numerical simulation

Chengwen Wang [a], Xiaoli Liu [a,*], Nan Hu [a], Wenli Yao [a], Enzhi Wang [a], Jianhong Jia [b]

[a] *Department of Hydraulic Engineering, State Key Laboratory of Hydroscience and Engineering, Tsinghua University, Beijing 100084, China*
[b] *YSD Rail Transit Construction Company Limited, Guangzhou 510630, China*

Received 5 February 2025; received in revised form 27 March 2025; accepted 12 May 2025
Available online 4 October 2025

Abstract

Twin-tunnel construction inevitably interacts under complex geological conditions, inducing highly complex hydraulic-rock-structure interactions. This study proposes a micro-electro-mechanical systems (MEMS)-based automatic monitoring system for in-situ measurement of rock and structural responses. It measures pore pressure, earth pressure, rock displacement, and additional stress and displacement of segments. Test results reveal three evolutionary stages: pre-shield arrival, shield passage, and post-shield passage. The final distribution and disturbance extent of these responses correlate with tunnel distance. A 3D refined numerical model incorporating the fluid–solid coupling and detailed construction process is developed. Numerical results analyze excess pore pressure, vault settlement, lining response, and key construction parameter effects (face and grouting pressure). Findings enhance understanding of twin tunnel interactions and hydraulic-rock-structural response mechanisms, providing insights for similar projects.

Keywords: Twin tunnels; In-situ measurement; Hydraulic-rock-structural responses; MEMS-based automatic monitoring system; Numerical simulation

1 Introduction

Rapid urbanization and population growth have driven extensive underground infrastructure development (Guo et al., 2021; Xie et al., 2021). At present, subway tunnels (Zhang et al., 2022; Jiang et al., 2021), water/power networks (Almheiri et al., 2021; Awaga et al., 2024; Barla & Insana, 2023), and defense projects, etc. occupy significant underground space. Earth pressure balance shield (EPBS) tunnelling is preferred for urban tunnels owing to its mechanization, speedy construction, geological adaptability, and environmental benefits (Cheng et al., 2019; Yin et al., 2018). Closely spaced twin tunnels are increasingly used to optimize investments and spatial layouts (Chortis & Kavvadas, 2021; Zheng et al., 2021). Interactions between adjacent twin tunnels are inevitable during construction (Chen et al., 2015; Gao et al., 2017). The disturbances to the surrounding rock, pore pressure, and reduced structural capacity in existing tunnels pose critical risks. These factors risk damaging new/existing tunnels and degrading serviceability, especially in high-pore-pressure environments. Thus, analyzing hydraulic-rock-structure responses in twin-tunnel construction is critical for geotechnical engineering.

Given geological complexity and EPBS-rock interactions, in situ monitoring effectively captures twin-tunnel interaction. Prior work focuses on excavation-induced ground displacement (Islam & Iskander, 2021; Wang et al., 2019). Furthermore, deep soil displacements (vertical/lateral) are also tracked via surface boreholes (Clayton et al., 2006). In-situ studies have examined pore pressure and existing tunnel responses (Bezuijen et al.,

* Corresponding author.
E-mail address: xiaoli.liu@tsinghua.edu.cn (X. Liu).
Peer review under the responsibility of Tongji University

https://doi.org/10.1016/j.undsp.2025.05.010

2001). Many studies reported monitoring pore pressure distribution during shield tunnelling via the hydrometer method (Han et al., 2017; Wan et al., 2019). Structural responses in existing tunnels include stress/deformation monitoring (Chen et al., 2018; Liu et al., 2022). Lining stress is typically monitored via strain gauges embedded during fabrication (Rauch & Fischer, 2024; H. Wu et al., 2024). Lining deformation is assessed using precision leveling or total stations (S. Wu et al., 2024). However, tunnel size, length, and poor lighting hinder these labor-intensive approaches. Incomplete field monitoring data necessitate numerical modeling. Numerical simulations effectively analyze strata deformation and tunnel interactions (Do et al., 2015). Studies employing finite element/finite difference methods-based 3D models investigate shield-induced strata deformation (Gu et al., 2024; Jia et al., 2024), pore pressure (Cui et al., 2023; Li et al., 2024), and lining responses (Allahverdi et al., 2023; Zheng et al., 2023). Numerical simulation accuracy depends on selecting an appropriate constitutive model and parameters. Underground engineering must consider true 3D stress states and adopt a compatible constitutive model, often overlooked in prior studies (Wang et al., 2023). Incorporating EPBS components and a detailed construction process is crucial for accurate shield tunnelling simulations.

The literature review indicates that Traditional methods face challenges in multi-parameter tunnel monitoring. MEMS-based sensors offer innovative solutions for multi-parameter monitoring. These sensors are compact, lightweight, precise, low-cost, energy-efficient, and highly integrable. Wireless compatibility further supports real-time automated monitoring. Given field monitoring limitations, comprehensive 3D numerical models integrating EPBS-hydraulic-rock-structure coupling are essential for analyzing twin-tunnel construction responses.

This paper introduces MFAS-TunRS, an innovative MEMS-based fusion automatic monitoring system for multi-parameter rock and structure monitoring in shield tunnels. An in-situ scheme monitors hydraulic-rock-structural responses in closely spaced twin tunnels. It tracks stress, deformation, and pore pressure in the surrounding rock, as well as additional stresses and displacements in the existing tunnel. A 3D refined numerical model of EPBS-hydraulic-rock-structure coupling is established to analyze hydraulic-rock-structural responses to construction perturbations and the effects of face and grouting pressures. These findings offer guidance for twin tunnel safety control and existing tunnel protection.

2 Project description

2.1 Site conditions

The Huangniupu-Huangjiang Center tunnel on Dongguan Metro Line 1 is in Huangjiang Town, Dongguan, China. It spans approximately 3.1 km in a north–south orientation, mainly enclosed by mountains (Fig. 1(a)). The study area comprises two parallel tunnels (left tunnel (LT) and right tunnel (RT)) spaced 14 m apart. To study rock and segmental lining behavior under deep burial and high pore pressure, the test site is set at Daling Mountain, the project's deepest section (Fig. 1(b)). The test section layout is shown in Fig. 1(c). The strata comprise four layers from the surface downward: plain fill, completely weathered sandstone, strongly weathered sandstone, and strongly weathered calcareous sandstone. The tunnels traverse strongly weathered calcareous sandstone at a 50 m burial depth, with groundwater at 21.5 m. Table 1 presents formation parameters from drilling and lab tests.

2.2 Shield tunnel conditions

The tunnel features a circular profile with an outer diameter of 6700 mm and an inner diameter of 6000 mm. The lining, measuring 35 cm in thickness and 1.5 m in width, consists of segments connected via staggered joints arranged in a "3 + 2 + 1" configuration (Fig. 2(a)). These segments are secured with M30-grade bending bolts, utilizing a total of 28 bolts per ring. Engineered with C50 concrete, the segments achieve an impermeability grade of P12. Construction employs two EPBS machines, each equipped with an excavation diameter of 6980 mm, and a main machine length of 9 m (Fig. 2(b)).

3 In-situ monitoring

3.1 Composition of the MFAS-TunRS automatic monitoring system

An automatic monitoring system, namely MFAS-TunRS, using MEMS sensors and wireless transmission technology, was designed to monitor shield tunnel rock and structural response. The MFAS-TunRS system (Fig. 3) consists of four components: segment and rock monitoring units, an intelligent gateway, and a data processing computer. The segment monitoring unit incorporates stress and tilt/displacement sensors. The stress sensor, with a high-precision strain gauge, transmits surface stress via a steel sheet fixed on the segment. The tilt/displacement sensor, with a triaxial accelerometer and magnetometer, measures segment tilt and joint displacement. The rock monitoring unit integrates displacement, pore pressure, and stress sensors, all encapsulated within a protective cover to ensure stability. The displacement sensors, with a triaxial accelerometer and magnetometer, monitor continuous formation displacement via data fusion. The piezoresistive sensor measures pore pressure (up to 3 MPa), while strain gauges detect earth pressure changes. Multiple rock monitoring units are interconnected via a three-degree-of-freedom hinge mechanism to form a linear measurement array within a single monitoring hole. Communication within the hole is facilitated by the RS-485

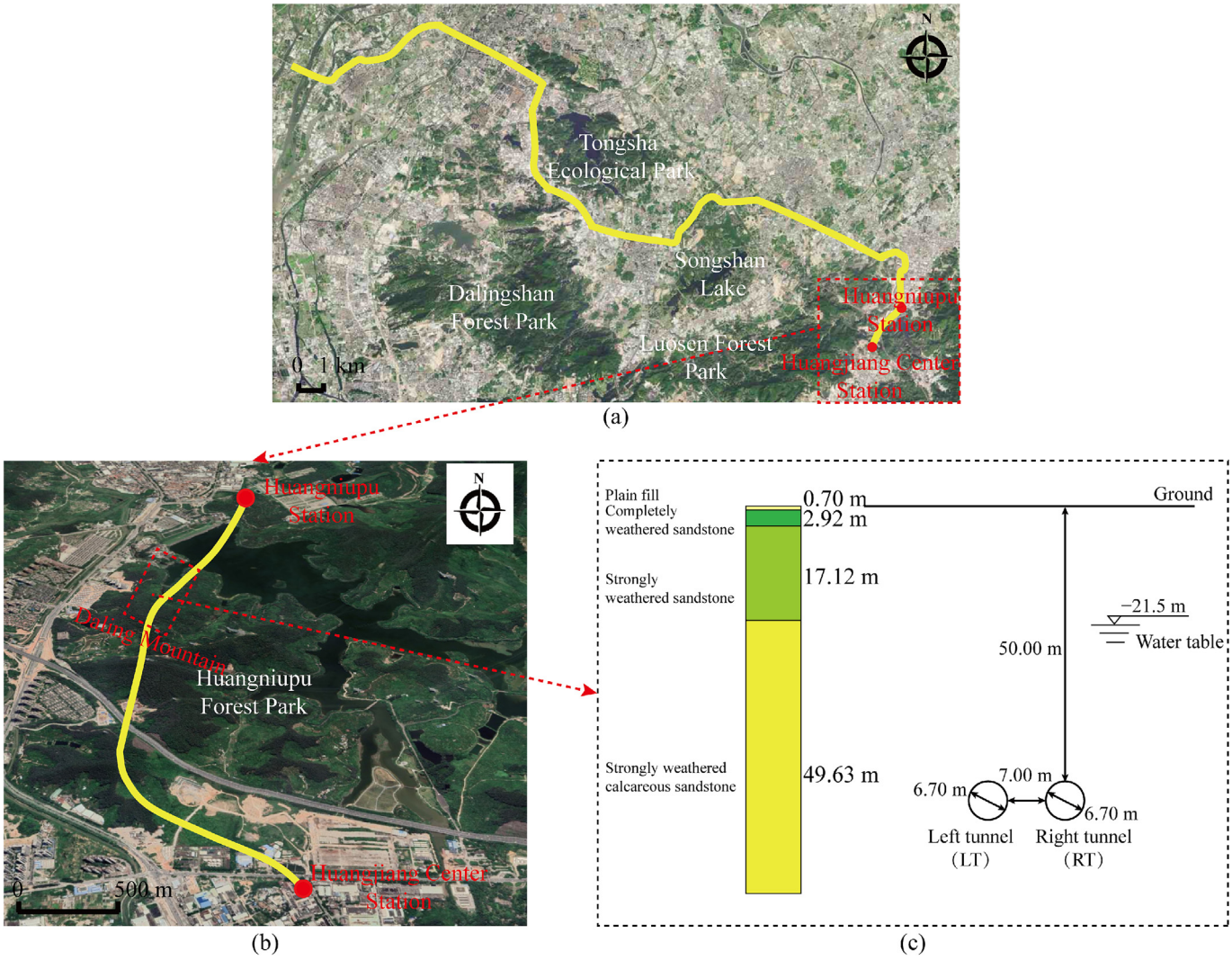

Fig. 1. General geological information of twin tunnels. (a) Location of study area, (b) plan of Dongguan Metro Line 1, and (c) profile view of monitoring section.

Table 1
Physical and mechanical parameters of strata in the study area.

Strata	Density (kg/m^3)	Compressive modulus (MPa)	Cohesion (kPa)	Friction angle (°)	Permeability coefficient (m/d)
Plain fill	1900	–	5	10	0.5
Completely weathered sandstone	1970	40	25	24	0.1
Strongly weathered sandstone	2000	80	40	25	0.5
Strongly weathered calcareous sandstone	2600	200	150	30	0.5

protocol, while data transmission between boreholes employs the LoRa wireless protocol. These units relay data to an intelligent gateway, which forwards it to a data processing computer for analysis and interpretation. It is worth noting that the sampling frequency in this study is set to once every two minutes. The synchronization of multi-node monitoring is achieved through absolute timestamps. Each dataset obtained from a monitoring node is assigned an absolute timestamp, and all data from multiple nodes are collectively transmitted to the wireless gateway. By utilizing absolute timestamps, synchronization across multiple nodes is ensured. The technical parameters of the MFAS-TunRS automatic monitoring system are summarized in Table 2.

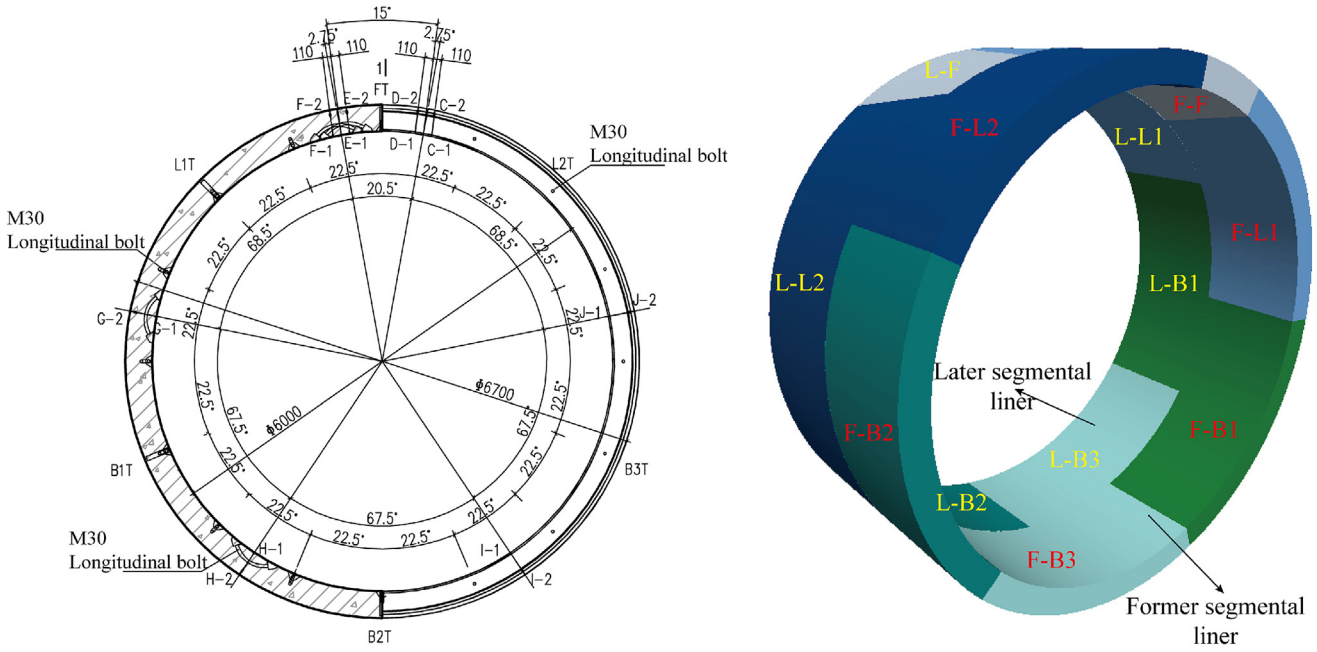

(a)

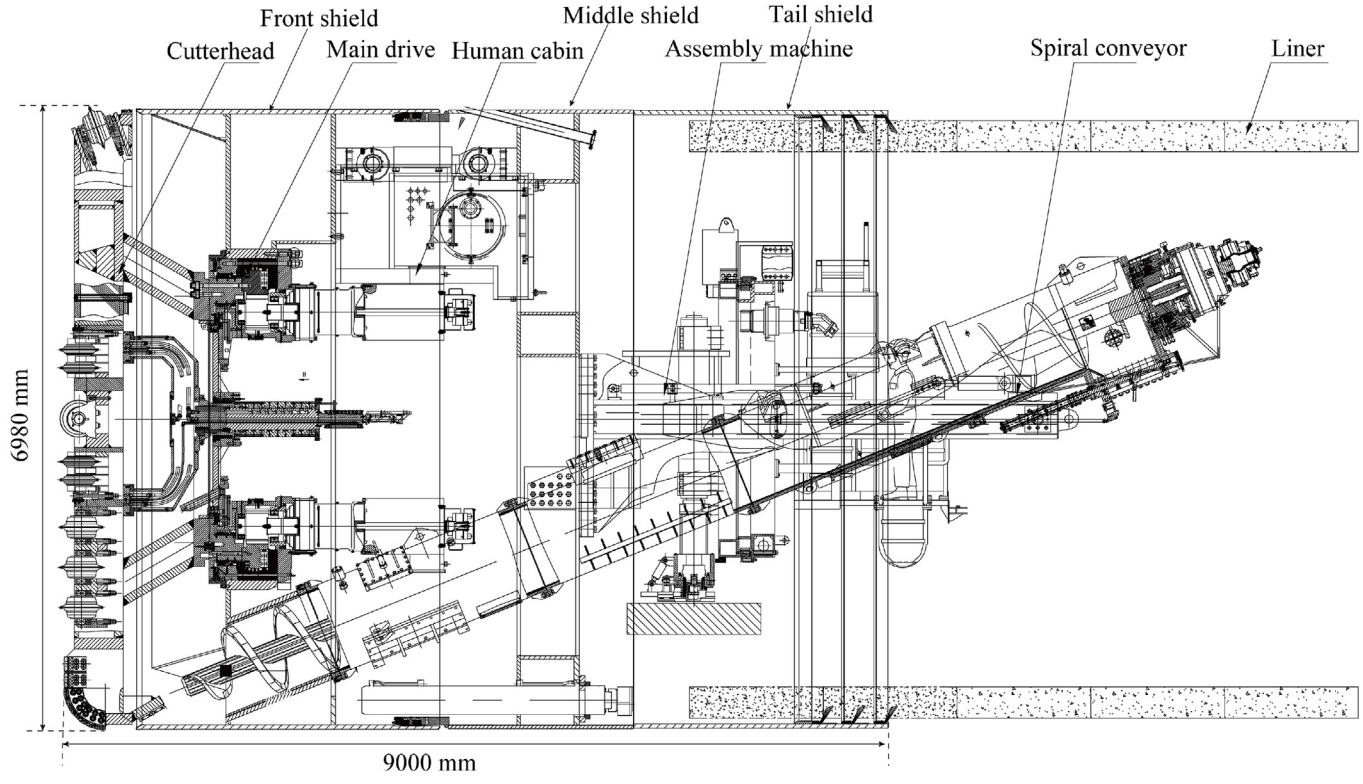

(b)

Fig. 2. Schematic diagrams of (a) segmental lining, and (b) EPBS machine.

3.2 Main monitoring principles of the MFAS-TunRS automatic monitoring system

For earth pressure, high-precision strain gauges are used for monitoring, and their internal structure is shown in Fig. 4(a). It is worth mentioning that the earth pressure monitoring sensor monitors the combined stress in the borehole direction. The monitoring system utilizes a piezoresistive pore pressure sensor to measure the pore pressure within the surrounding rock, as depicted in

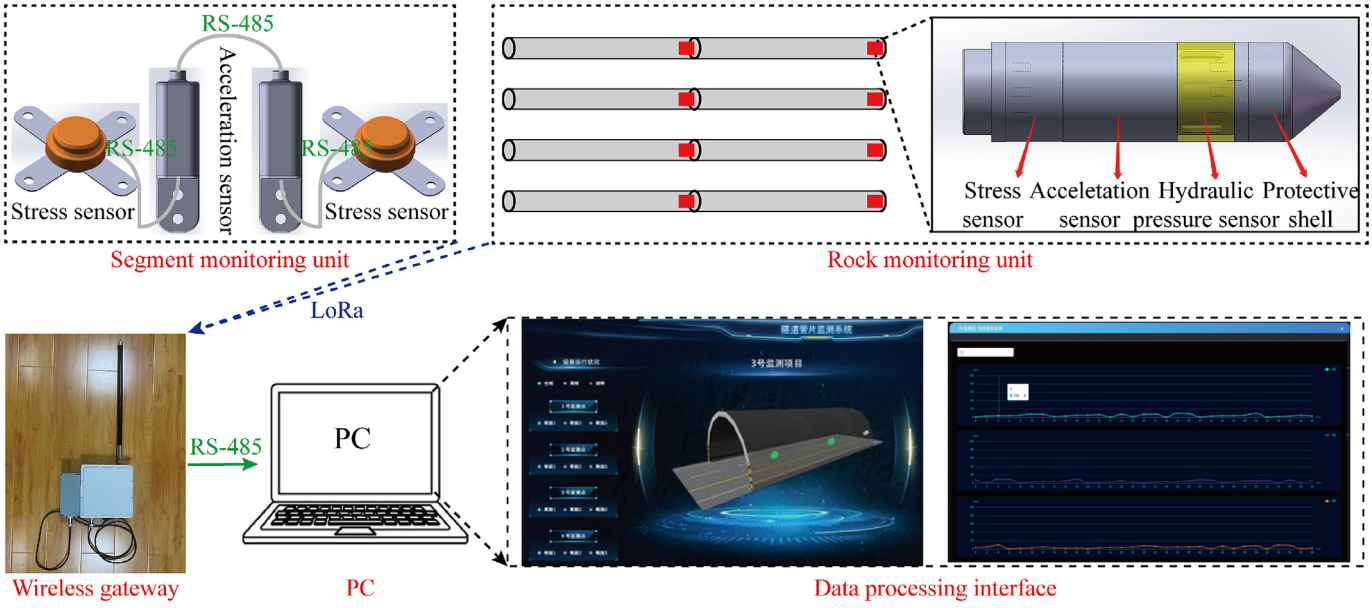

Fig. 3. Schematic diagram of the MFAS-TunRS automatic monitoring system.

Table 2
Technical parameters of the MFAS-TunRS automatic monitoring system.

Device	Technical parameter	Value
Stress sensor	Sensitivity coefficient	2.1 ± 1%
	Strain limit	2500 μm/m
	Mechanical lag	1.1 μm/m
	Temperature range	–20 to 60 ℃
	Fatigue life	10 million times
Acceleration sensor	Acceleration range	±2*g* to ± 8*g*
	Acceleration accuracy	3.9 μg
	Temperature drift	±0.02 mg/℃
	Linearity	0.1%FS
	Tilt accuracy	0.1°
Pore pressure sensor	Measuring range	0–3000 kPa
	Precision	±0.5 kPa
	Resolution	0.1 kPa
Wireless gateway	Wireless communication mode	LoRa
	Frequency band	433 MHz
	Receiving sensitivity	–129 dBm
	Transmit power	22 dBm
	Communication distance	>3.5 km (open environment)
	Data transmission rate	1.2 kbps

Note: The technical parameters of stress sensors used in the rock monitoring unit and segment monitoring unit are the same as those of acceleration sensors. *g* refers to gravity acceleration.

Fig. 4(b). The internal displacement of the surrounding rock is monitored through the integration of a triaxial accelerometer and a triaxial magnetometer. As illustrated in Fig. 4(c), using a high-precision triaxial accelerometer for measurements within the local spatial frame yields three precise gravity vector components, incorporating two key parameters: the pitch angle (α) and the roll angle (β).

$$\begin{cases} \alpha = \arctan\left(\frac{a_x}{a_y}\right) \\ \beta = \arctan\left(\frac{\sqrt{a_x^2+a_y^2}}{a_z}\right) \end{cases}, \quad (1)$$

where a_x, a_y, and a_z are the accelerations in the three directions measured by the triaxial accelerometer, respectively. The yaw angle (θ) in the plane orthogonal to the direction

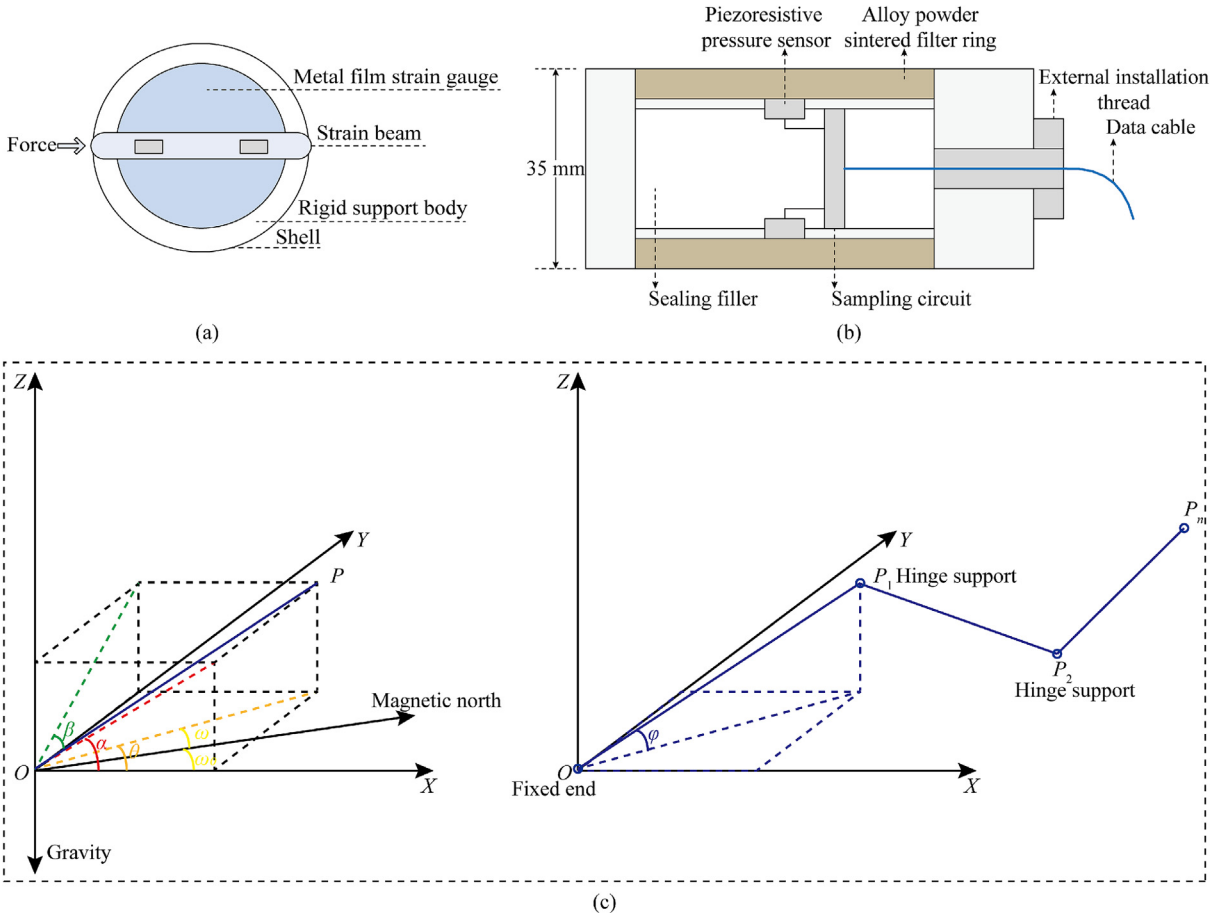

Fig. 4. Main monitoring principles of the MFAS-TunRS automatic monitoring system: (a) earth pressure monitoring sensor structure, (b) piezoresistive pressure sensor structure, and (c) principle of rock displacement fusion solution.

of gravity is measured using a triaxial magnetometer. Measurement in localized space using a high-precision triaxial magnetometer yields three high-precision magnetic field components, providing two accurate pieces of information: yaw angle (θ) and pitch angle (α). The yaw angle should be corrected for attitude according to the pitch and roll angles of the measurement system.

$$\begin{cases} M_x = M_x^* \cos\alpha + M_y^* \sin\beta \sin\alpha - M_z^* \cos\beta \sin\alpha \\ M_y = M_y^* \cos\beta + M_z^* \sin\beta \end{cases}, \tag{2}$$

where M_x and M_y are the corrected magnetic components in the x and y directions, respectively; M_x*, M_y*, and M_z* are the magnetic components in the three directions measured by the triaxial magnetometer, respectively.

$$\theta = \begin{cases} 90^\circ, \ M_x < 0 \text{ and } M_y < 0, \\ 180^\circ - \arctan(M_y/M_x), \ M_x < 0 \text{ and } M_y > 0, \\ 270^\circ, \ M_x = 0 \text{ and } M_y > 0, \\ -\arctan(M_y/M_x), \ M_x > 0 \text{ and } M_y < 0, \\ 360^\circ - \arctan(M_y/M_x), \ M_x > 0 \text{ and } M_y > 0. \end{cases} \tag{3}$$

The rock displacement is determined based on the known attitude parameters: pitch angle (α), roll angle (β), and yaw angle (θ). As shown in Fig. 4(c), the angle φ between OP_1 and the XOY plane is:

$$\varphi = \arctan(\tan\alpha \cos\theta). \tag{4}$$

Assume that the length of OP_1 is L_1 (a known parameter). The coordinates of P_1 at time t are:

$$\begin{bmatrix} P_{1x} \\ P_{1y} \\ P_{1z} \end{bmatrix} = L_1 \begin{bmatrix} \cos\varphi \cos\theta \\ \cos\varphi \sin\theta \\ \sin\varphi \end{bmatrix}. \tag{5}$$

Assuming the coordinates of point P_1 time $t + 1$ are (P_{1x}*, P_{1y}*, P_{1z}*), the displacement of P_1 relative to the origin O is:

$$\begin{bmatrix} \Delta x_{P1} \\ \Delta y_{P1} \\ \Delta z_{P1} \end{bmatrix} = \begin{bmatrix} P_{1x}^* \\ P_{1y}^* \\ P_{1z}^* \end{bmatrix} - \begin{bmatrix} P_{1x} \\ P_{1y} \\ P_{1z} \end{bmatrix}. \tag{6}$$

Assuming that position of point P_2 is written as (P_{2x}*, P_{2y}*, P_{2z}*) at time $t + 1$, then:

$$\begin{bmatrix} \Delta x_{P2} \\ \Delta y_{P2} \\ \Delta z_{P2} \end{bmatrix} = \begin{bmatrix} P^*_{2x} \\ P^*_{2y} \\ P^*_{2z} \end{bmatrix} - \begin{bmatrix} P_{2x} \\ P_{2y} \\ P_{2z} \end{bmatrix}. \quad (7)$$

Similarly, assuming that the position of point P_n is written as (P_{nx}*, P_{ny}*, P_{nz}*) at time $t + 1$, then:

$$\begin{bmatrix} \Delta x_{Pn} \\ \Delta y_{Pn} \\ \Delta z_{Pn} \end{bmatrix} = \begin{bmatrix} P^*_{nx} \\ P^*_{ny} \\ P^*_{nz} \end{bmatrix} - \begin{bmatrix} P_{nx} \\ P_{ny} \\ P_{nz} \end{bmatrix}. \quad (8)$$

The monitoring principle of the segment monitoring unit is similar to that of the rock monitoring unit and is described in detail in Wang's work (Wang et al., 2024a).

3.3 Arrangement of the monitoring system

During twin tunnel construction, the left tunnel (LT) was excavated first, with the right tunnel (RT) lagging by 100 m. To assess RT excavation impacts on the surrounding rock and segments, the monitoring system was installed in LT. After advancing LT's shield machine to the test section, horizontal directional drilling created monitoring holes on both sides of the segment (Fig. 5(a)). Monitoring boreholes were drilled horizontally into the surrounding rock through pre-reserved segment grouting holes. Each 40 mm-diameter, 2 m-deep borehole housed a 30 mm-diameter rock monitoring unit. The 2 m-long unit incorporated MEMS sensors spaced at 1 m intervals. Four monitoring points (ML1, ML2, MR1, MR2) tracked surrounding rock disturbance. A segment monitoring unit (MS) was secured near RT using expansion screws. As presented in Fig. 5(b), the monitoring system's implementation steps can be delineated as follows: (1) Horizontal directional drilling was used to drill into the surrounding rock on both sides of the tunnel and at the reserved grouting holes in lining to form monitoring holes; (2) Position the surrounding rock monitoring unit onto the specified location within the monitoring hole; (3) Utilize epoxy resin for coupling grouting, and rapidly setting cement for hole sealing; (4) Position and secure the segment monitoring

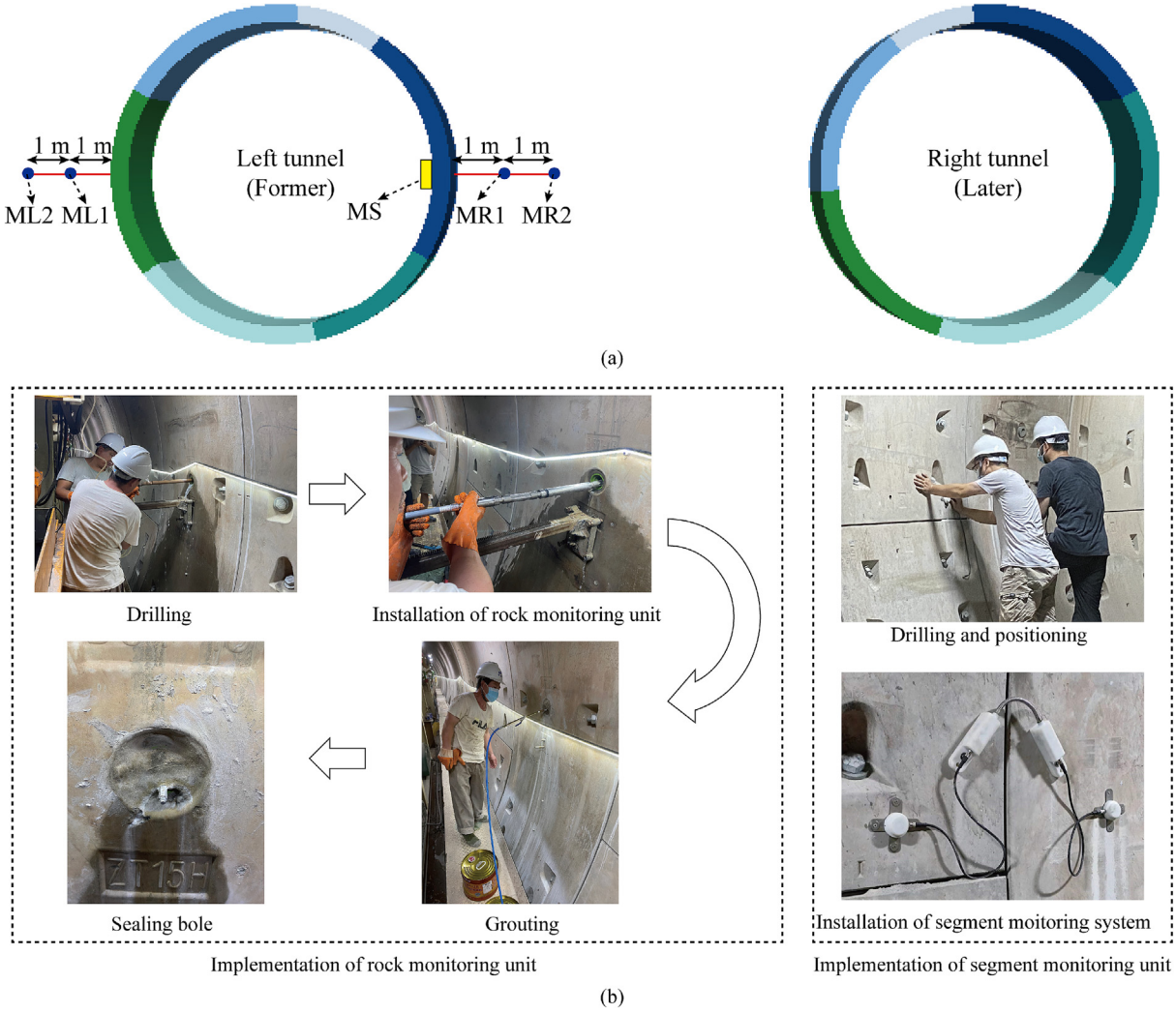

Fig. 5. Arrangement of the monitoring system. (a) Layout of monitoring points, and (b) installation process of the monitoring system.

unit with expansion screws at the predetermined location of the segment using a handheld drill; (5) Dangle the wireless gateway on the segment, and assess the wireless gateway's signal reception quality; (6) Upon reaching the test section, with the initiation of measurement, RT is propelled forward. Monitoring was initiated on July 24, 2022, and culminated on August 4, 2022, during which RT advanced by 63 rings (94.5 m).

3.4 In-situ monitoring results

3.4.1 Pore pressure

Figure 6 depicts the evolution of pore pressure surrounding the first tunnel as the EPBS traversed the testing section. The monitoring procedure was divided into three stages: Stage I involved the period before the EPBS tunnelling face of RT reached the monitoring section; Stage II encompassed the period during which the EPBS passed through the monitoring section; and Stage III encapsulated the period following the EPBS's traversal of the monitoring section. It is evident that the pore pressure underwent different developmental trajectories at the far end (i.e., the left side of LT, ML1, and ML2) and the near end (i.e., between the twin tunnels, MR1 and MR2).

Furthermore, Fig. 6 depicts the pore pressure evolution at each of the four monitoring points, demonstrating a similar pattern of change. During Stage I, pore pressure reduced exponentially and entered the first stabilization phase during the EPBS's shutdown maintenance in the second tunnel. In Stage II, pore pressure underwent a significant sudden drop, followed by entering the second stabilization phase, which is still linked to the shield shutdown. The decline in pore pressure was significantly greater at MR1 and MR2 than at ML1 and ML2. In Stage III, pore pressure experienced a sudden drop at ML1 and ML2, followed by entering the stabilization phase, mainly related to the shield tail dragging out. Conversely, at MR1 and MR2, pore pressure underwent a sudden decline, followed by a subsequent rise, and ultimately entered the stabilization phase. This pattern is mainly due to the shield tail grouting effect, which did not transmit to ML1 and ML2 due to the existing tunnel structure barrier. In summary, pore pressure underwent three significant drops throughout the monitoring process and ultimately remained at a relatively low value. The primary cause could be attributed to the low earth chamber pressure set for the EPBS, which was aimed at efficient tunnelling in hard rock. As a result, the excavation of the second tunnel created a fresh outlet for groundwater discharge and led to a dissipation of pore pressure. After stabilization, due to the low permeability of the rock, it is difficult to quickly recover the pore pressure during the monitoring period.

The pore pressure distribution and variation across the three stages are presented in Fig. 7. It is evident that the final pore pressure at the far end exceeds that at the near end. Specifically, at the far end, the final pore pressure recorded at ML2 is higher than that at ML1, which is attributed to the disturbance caused by the first excavation. The second excavation at the near end resulted in a significant disturbance effect, with the final pore pressure recorded at MR1 and MR2 being almost the same. The final pore pressure was ranked as ML2 > ML1 > MR2 > MR1, primarily determined by the disturbance caused by the first excavation and the distance from the second tunnel. Regarding the variations in pore pressure during the monitoring period, it can be observed that in Stage I, pore pressure experienced a significant decrease, with the magnitude of the decrease being MR2 = MR1 > ML1≈ML2 at the four monitoring points. In Stage II, the dissipation of pore pressure at ML1 and ML2 was considerably lower than that at MR1 and MR2, with the ranking of pore pressure change being MR2 = MR1 > ML1 > ML2, which is positively correlated with the distance from the second tunnel. In Stage III, pore pressure

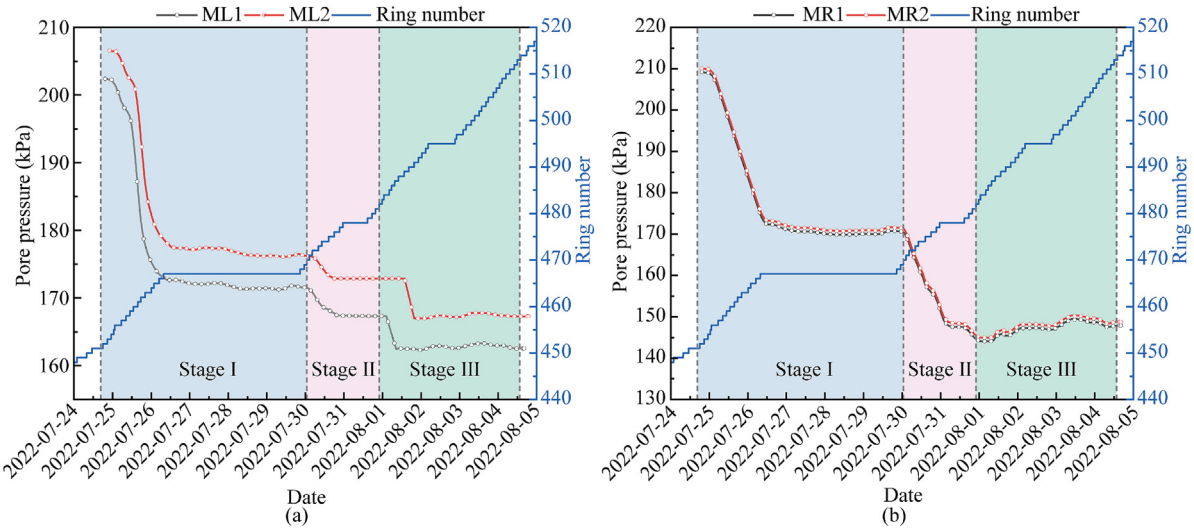

Fig. 6. Development history of pore pressure: (a) pore pressure at the far end, and (b) pore pressure at the near end.

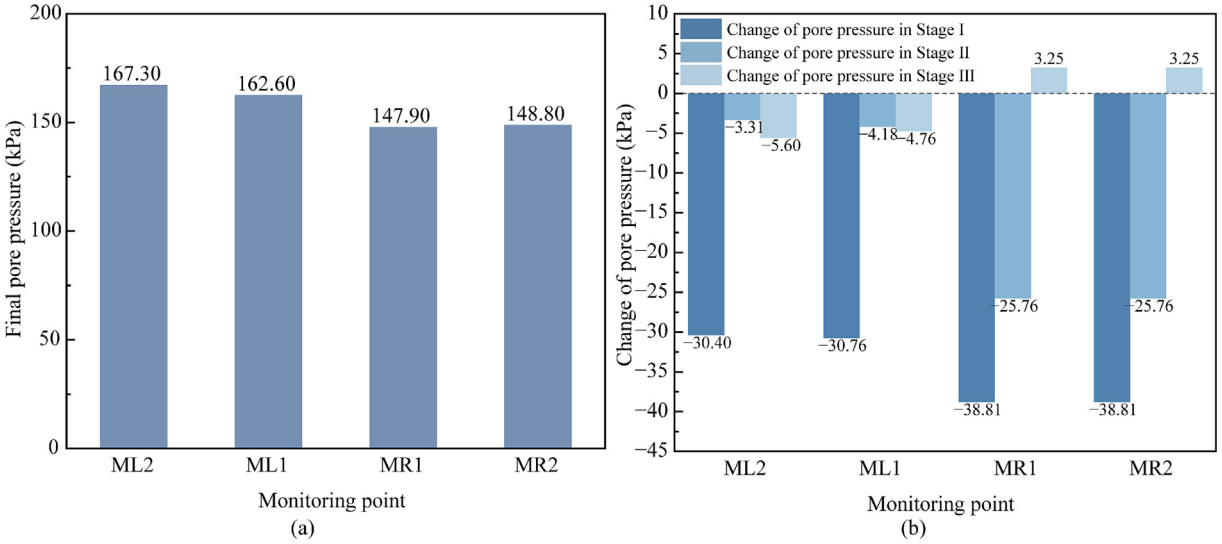

Fig. 7. Characteristics of pore pressure: (a) final pore pressure, and (b) change of pore pressure.

decreased at the far end while increasing at the near end, mainly due to the ineffectiveness of grouting at the far end as a result of the barrier effect of the existing tunnel structure.

3.4.2 Earth pressure

Figure 8 shows the earth pressure development at four monitoring points, where the envelope stresses are combined horizontally, with positive values indicating compressive stresses. The earth pressure at the far and near ends has different developmental patterns. As shown in Fig. 8(a), at the far end, the earth pressure development at points ML1 and ML2 is similar. In Stage I, the earth pressure increases rapidly, mainly due to the continuous pressure on the tunnel face in RT, causing lateral extrusion of the surrounding rock. In Stage II, the earth pressure increases slowly. The excavation of the second tunnel releases stresses, but the far-end stresses are not released due to the structure support in the first tunnel. In Stage III, as the excavation face of the second tunnel gradually moved away from the monitoring section, the earth pressure at the far end stabilized. Throughout the process, the earth pressure at ML1 is consistently smaller than at ML2 because ML1 is closer to LT. The stress release during the first excavation is larger, making the stress at ML1 always smaller than at ML2 during the second excavation. Figure 8(b) shows that at the near end, the earth pressure at MR1 and MR2 follows different evolutionary processes. In Stage I, the earth pressure increases exponentially due to lateral compression from the second tunnel's face pressure. In Stage II, the earth pressure at MR1 increases slowly, while at MR2 it decreases dramatically. Compared to MR1, MR2 is closer to the newly excavated tunnel and thus more strongly disturbed. The excavation and unloading of RT cause rapid stress release at MR2. The different stress responses at MR1 and MR2 indicate that the excavation and unloading of the newly-built tunnel have a limited scope, with MR1 not being significantly affected. Overall, the near end is more affected by the disturbance from the secondary excavation. In Stage III, the stress at MR1 quickly stabilizes, while at MR2 it rebounds rapidly. As the tunnel face in RT moves away from the monitoring section, the earth pressure at MR2 gradually stabilizes due to unchanged force and boundary conditions. Initially, the earth pressure at MR2 is slightly larger than at MR1 due to different degrees of unloading from the first excavation. The stress release at MR1 is more significant than at MR2 after the first excavation. As the second tunnel was excavated, MR2, being closer to the tunnel, experienced a drastic stress release, resulting in lower stress at MR2 compared to MR1.

Figure 9(a) illustrates the final distribution of earth pressure. At ML1 and ML2, which are far from the newly-built tunnel and supported by the lining structures in the first tunnel, the final earth pressure is higher due to less disturbance from the secondary excavation. At MR1, which is at the near end but farther from the newly-built tunnel, the final earth pressure is comparable to that at ML1. The final earth pressure at MR2 is smaller due to significant secondary disturbance and strong unloading effects. The final earth pressure at the four monitoring points is ordered as ML2 > ML1 ≈ MR1 > MR2, showing a positive correlation with the distance to the newly-built tunnel. Figure 9(b) shows the three stages of earth pressure variation. In Stage I, the earth pressure at all four monitoring points increases. The changes are ordered as MR1 > ML1 > MR2 > ML2, almost symmetrically distributed along the first tunnel sides, indicating a greater influence from the first tunnel. In Stage II, the earth pressure at MR2 decreases, while it slightly increases at ML1, ML2, and MR1. The changes are ordered as MR2 > MR1 > ML1 ≈ ML2. The lining structure of the first tunnel isolates

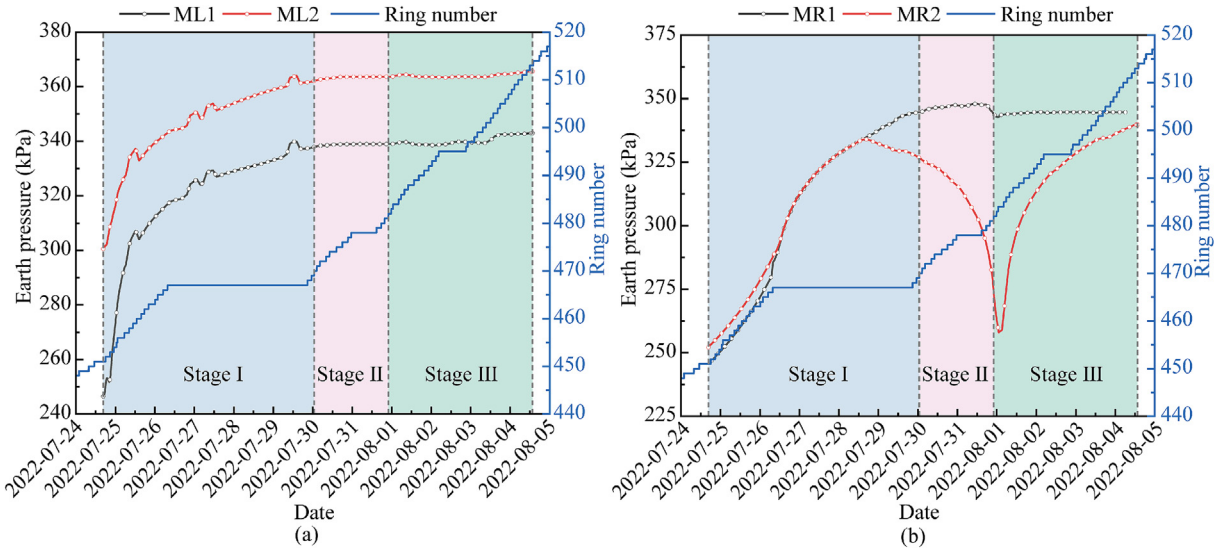

Fig. 8. Development history of earth pressure: (a) earth pressure at the far end, and (b) earth pressure at the near end.

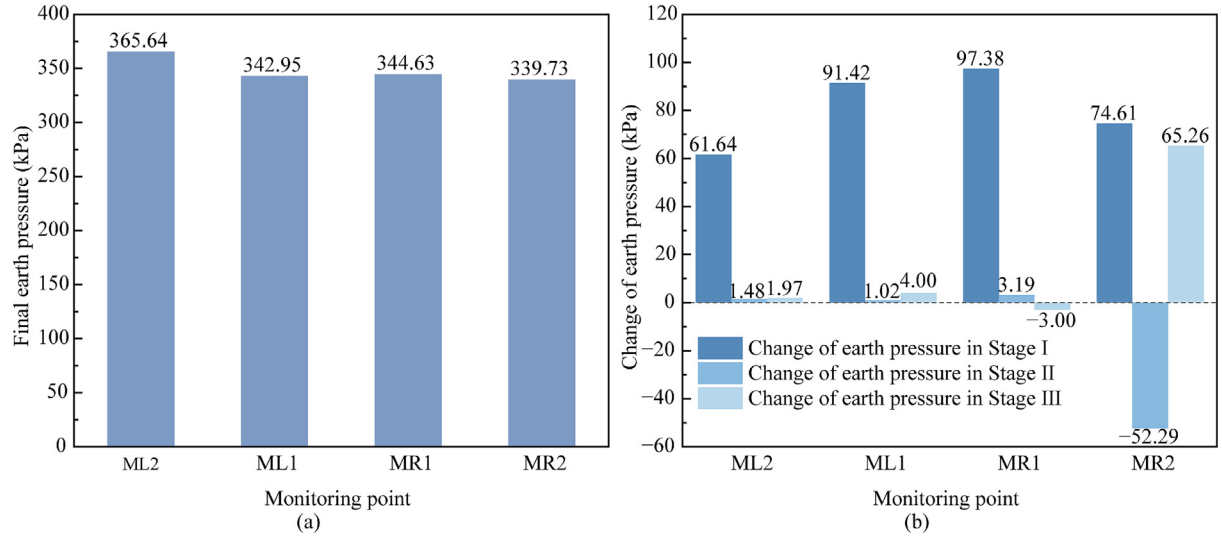

Fig. 9. Characteristics of earth pressure: (a) final earth pressure, and (b) change of earth pressure.

responses on both sides, preventing the unloading effect of the second tunnel from reaching the far end. Thus, changes in earth pressure at ML1 and ML2 are minimal. The stress change at MR1 is not significant due to its distance from the second tunnel, while MR2 experiences significant stress release. In Stage III, except for MR2, where the stresses recovered considerably, the earth pressure at the other three points remained stable.

3.4.3 Rock displacement

To simplify the presentation, the rock displacements at the four monitoring points were converted into a Cartesian coordinate system for unified analysis. Figure 10 shows the development of rock displacement in three directions. It can be seen that the rock displacements at the four monitoring points follow a similar evolutionary process. In the *x*-direction (radial) and *z*-direction (vertical): Stage I, the rock displacement increased rapidly. The increase was not affected by the downtime of the second tunnel, indicating a time-delayed effect of excavation disturbance on rock displacement, related to the continuous excavation of the first tunnel. In Stage II, the rate of increase of rock displacement slowed. Due to the lining support of the existing tunnel, the displacement at the far end nearly stopped increasing, and at ML2 showed obvious fluctuation but minimal overall growth. The near end, directly connected with the second tunnel and lacking support structure protection, continued to increase in displacement. In Stage III, the rock displacement gradually entered the stabilization stage after a slow increase. In the *y*-direction (longitu-

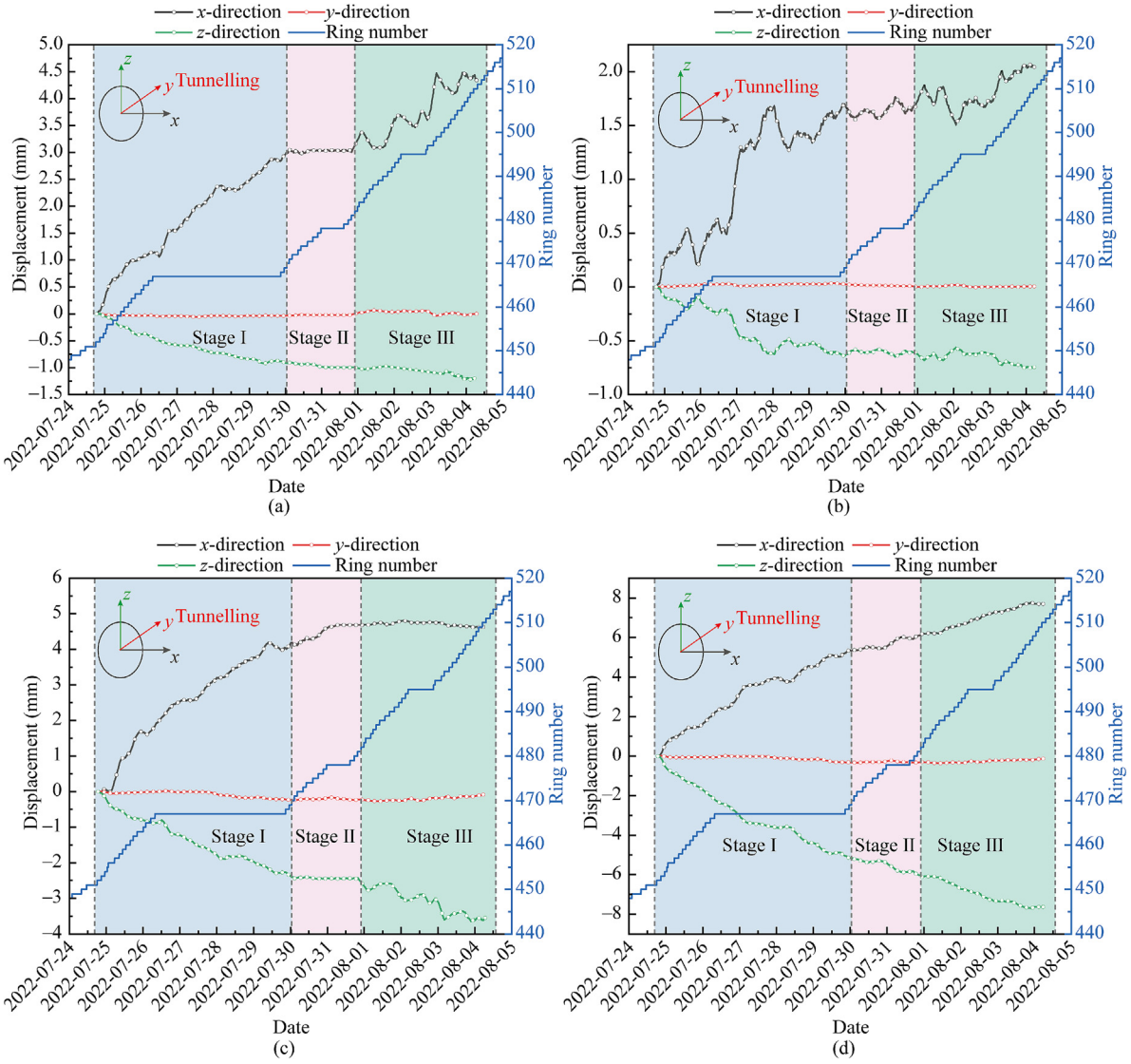

Fig. 10. Development history of rock displacement at (a) ML1, (b) ML2, (c) MR1, and (d) MR2.

dinal), the change in rock displacement during the entire monitoring process is very small and almost negligible. The magnitude of rock displacement by direction is: x-direction (radial) > z-direction (vertical) > y-direction (longitudinal). The x-direction is mainly affected by the excavation and unloading of the second tunnel, making it the largest displacement. The z-direction is influenced by gravity and lateral unloading, making it the second largest. The y-direction is mainly affected by friction between the shield shell and surrounding rock, showing minimal change during monitoring. The development trend of rock displacement aligns with the findings of previous numerical studies (Wang et al., 2024b; Zhou et al., 2018).

Figure 11(a) shows the distribution of final rock displacement. The total final displacements at the four monitoring points are in descending order: MR2 > MR1 > ML1 > ML2, inversely proportional to the distance to the second tunnel. The total displacement at MR2 is much larger than at the other three points, mainly because MR2 is closest to the second tunnel and thus significantly affected by the disturbance from secondary excavation. Conversely, the ML1 and ML2, far from the second tunnel and supported by the existing tunnel lining structure, did not experience large displacement. As shown in Fig. 11(b), regarding components of rock displacement, the relationship at each monitoring point is x-direction (radial) > z-direction (vertical) > y-direction (longitudinal). The longitudinal displacement is small at all four points. The closer the monitoring points are to the second tunnel, the smaller the difference between displacement in the x- and z-directions, indicating a more significant lateral unloading effect near the newly-built tunnel. This effect brings not only lateral displacement but also increases vertical settlement near the existing tunnel. Figure 11(c) illustrates the variation of rock displacement across the three monitoring stages. From the perspective of monitoring point locations,

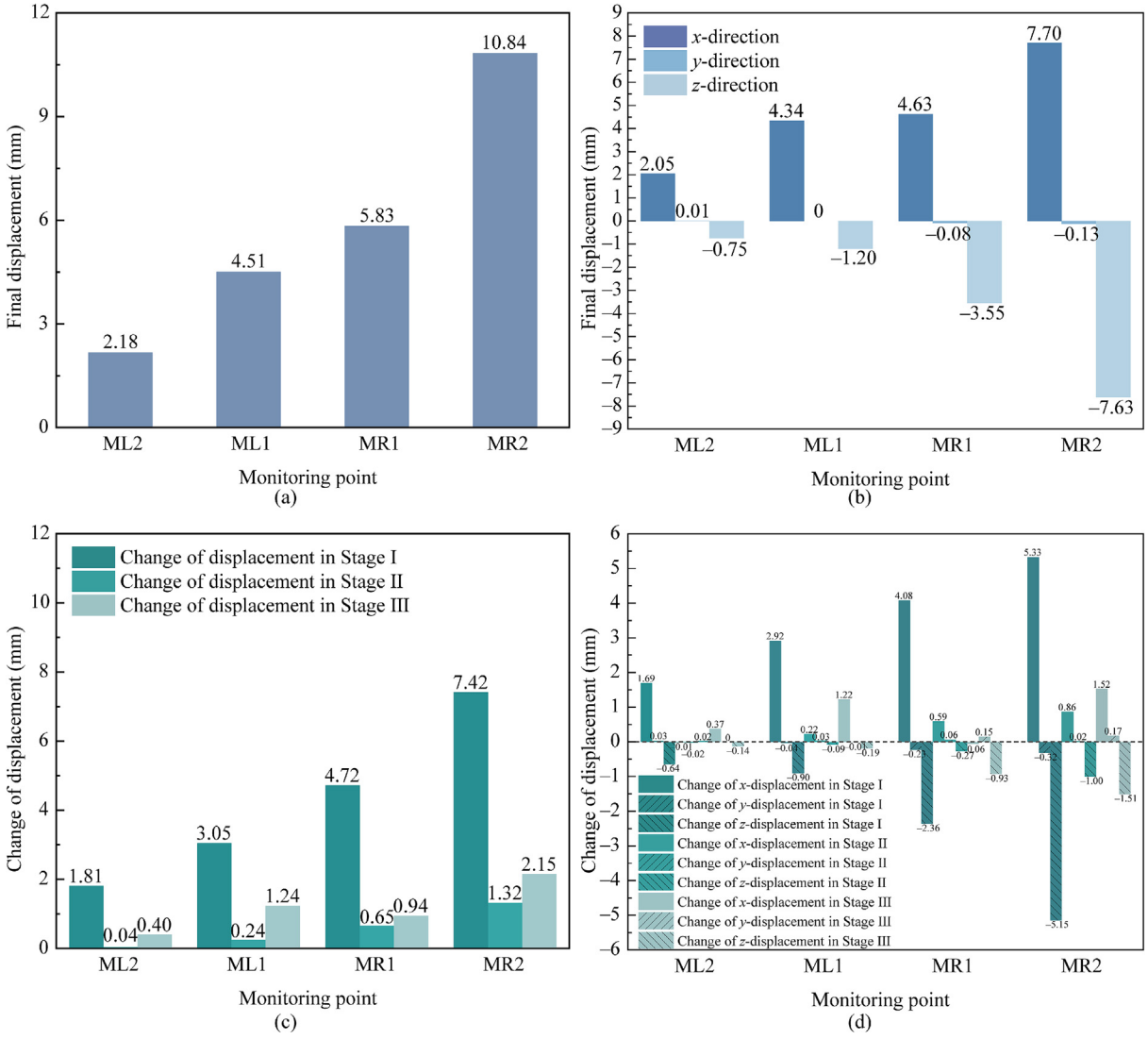

Fig. 11. Characteristics of (a) distribution of final rock displacement, (b) distribution of rock displacement components, (c) change of final rock displacement, and (d) changes of rock displacement components.

the total displacement at each stage follows the order: MR2 > MR1 > ML1 > ML2. At each monitoring point, the total displacement variation follows the order: Stage I > Stage III > Stage II. Most rock displacement occurs before the shield arrives in the second tunnel. During the shield passage stage, the support from the shield shell is evident, leading to minimal rock displacement. Rock displacement after shield passage is inversely proportional to the distance from the second tunnel. Regarding displacement components, as shown in Fig. 11(d), in Stage I and Stage II, the x-direction displacement is the largest, followed by the z-direction, with the y-direction displacement being very small. During these two stages, the surrounding rock is primarily affected by the lateral unloading from the excavation of the second tunnel, resulting in significant x-direction displacement. Additionally, the lateral unloading promotes vertical settlements of the surrounding rock around the first tunnel. Combined with the effect of gravity, this leads to a relatively large vertical displacement. In Stage III, z-direction displacement is predominant, followed by x-direction displacement. As the second tunnel face moves away from the monitoring section, the influence of lateral unloading weakens, and vertical settlement due to gravity becomes the dominant factor in rock displacement.

3.4.4 Additional stress and relative displacement of the segment

Figure 12 depicts the segment's additional stress at MS and its corresponding values (with positive values indicating compressive stress). Both axial and circumferential additional stress exhibit the same trend. In Stage I, additional stress experienced rapid growth until two rings before the EPBS's arrival, when it decreased due to the temporary support provided by the face pressure. In Stage

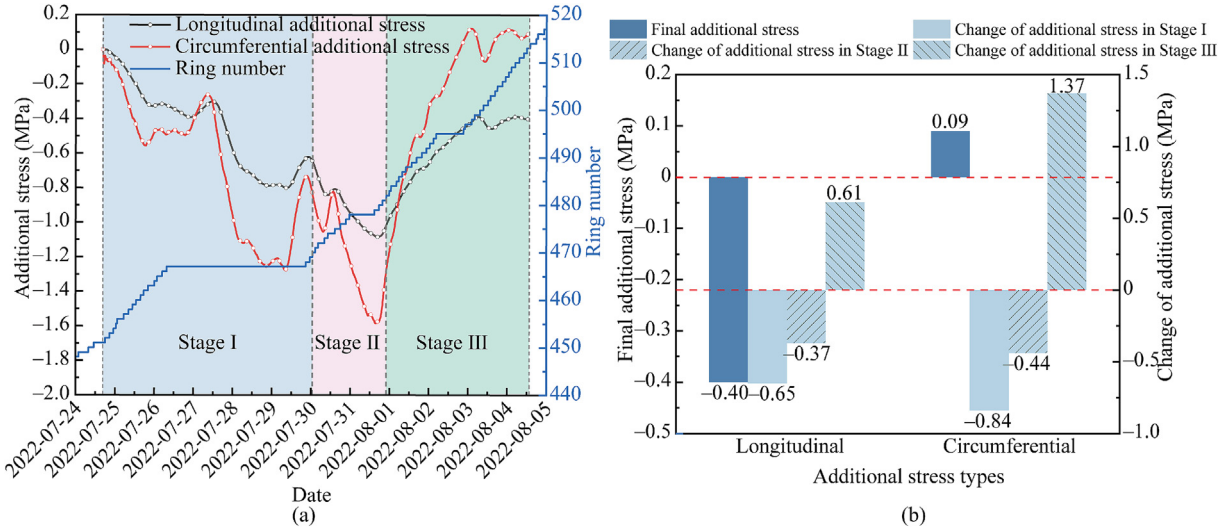

Fig. 12. Additional stress of segment at MS: (a) evolutionary process, and (b) characteristic values.

II, additional stress fluctuated but experienced an overall sharp increase. In Stage III, additional stress decreased rapidly and entered the stabilization phase gradually. Throughout the monitoring process, both axial and circumferential additional stress were primarily tensile stress. The final axial additional stress was –0.4 MPa, and the final circumferential additional stress was 0.09 MPa. The change in circumferential additional stress was larger than that of axial additional stress in each stage, suggesting that the lateral unloading effect brought by the excavation of the right tunnel is the primary factor contributing to the additional stress of the existing tunnel's segment.

Figure 13 shows the relative displacement of the lining segments at MS and their characteristic values. In the *x*- and *y*- directions, the development pattern of the relative displacement of the lining segments is basically the same: Stage I increases rapidly, Stage II decreases, and Stage III slowly increases to stabilize. The *z*-direction relative displacement shows a small, continuous increase throughout. From Fig. 13(b), it can be seen that the relative displacement at MS is mainly characterized by: outward displacement (toward the direction of the second tunnel) in the *x*-direction, tensioning in the *y*-direction, and downward displacement in the *z*-direction. The final relative displacement follows the relationship: *x*-direction>*y*-direction >*z*-direction. The changes in relative displacement during the three stages are also dominated by *x*-direction displacement, followed by *y*-direction displacement, with *z*-direction displacement being the smallest. The relative displacement is largest in Stage I, followed by Stage III and Stage II. In Stage I, the relative displacement in the first tunnel changes significantly as the face of the second tunnel approaches. In Stage II, the second tunnel is supported by the shield shell, minimizing the relative displacement in the first tunnel. In Stage III, after stress release caused by the excavation of the second tunnel, the redistribution of stress in the surrounding rock causes significant changes in the relative displacement in the first tunnel. Once a stable support structure is formed in the second tunnel, the relative displacement gradually stabilizes.

4 Numerical simulation

4.1 3D refined numerical model and verification

A refined 3D numerical model of an EPBS twin tunnels, based on the fluid–solid coupling theory, was established using FLAC3D. For simplicity, the modeling area is selected within the sandstone range. As shown in Fig. 14, the model size is set to 140 m × 120 m × 60 m to eliminate boundary effects (Lambrughi et al., 2012). The model contains 1 274 400 zones and 1 279 081 nodes. Based on previous experience (Do et al., 2015; Wang et al., 2024b), such a grid density is sufficient to ensure the accuracy. The bottom is fixed and impermeable. All vertical boundaries are constrained against horizontal displacement with constant pore pressure. The top is a free boundary with 486 kPa vertical stress and 20 kPa fixed pore pressure. The 3D rock mass response was simulated using FLAC3D with the generalized nonlinear unified strength theory (GNUST) model (Wang et al., 2023), extending the Hoek–Brown criterion to account for intermediate principal stresses. Its yield function is expressed as Eq. (9). The GNUST model was coded in C++, compiled into a FLAC3D-compatible dynamic link library (DLL), and integrated for simulations.

$$F=\begin{cases} f=\left(\sigma_1-\frac{b\sigma_2+\sigma_3}{1+b}\right)-\sigma_{ci}\left[m_b\frac{b\sigma_2+\sigma_3}{(1+b)\sigma_{ci}}+s\right]^a, & f\le f' \\ f'=\left(\frac{\sigma_1+b\sigma_2}{1+b}-\sigma_3\right)-\sigma_{ci}\left[m_b\frac{\sigma_3}{\sigma_{ci}}+s\right]^a, & f>f' \end{cases}, \tag{9}$$

where σ_{ci} is intact rock unconfined strength; m_b, s, and a are the rock mass parameters; and b is the coefficient.

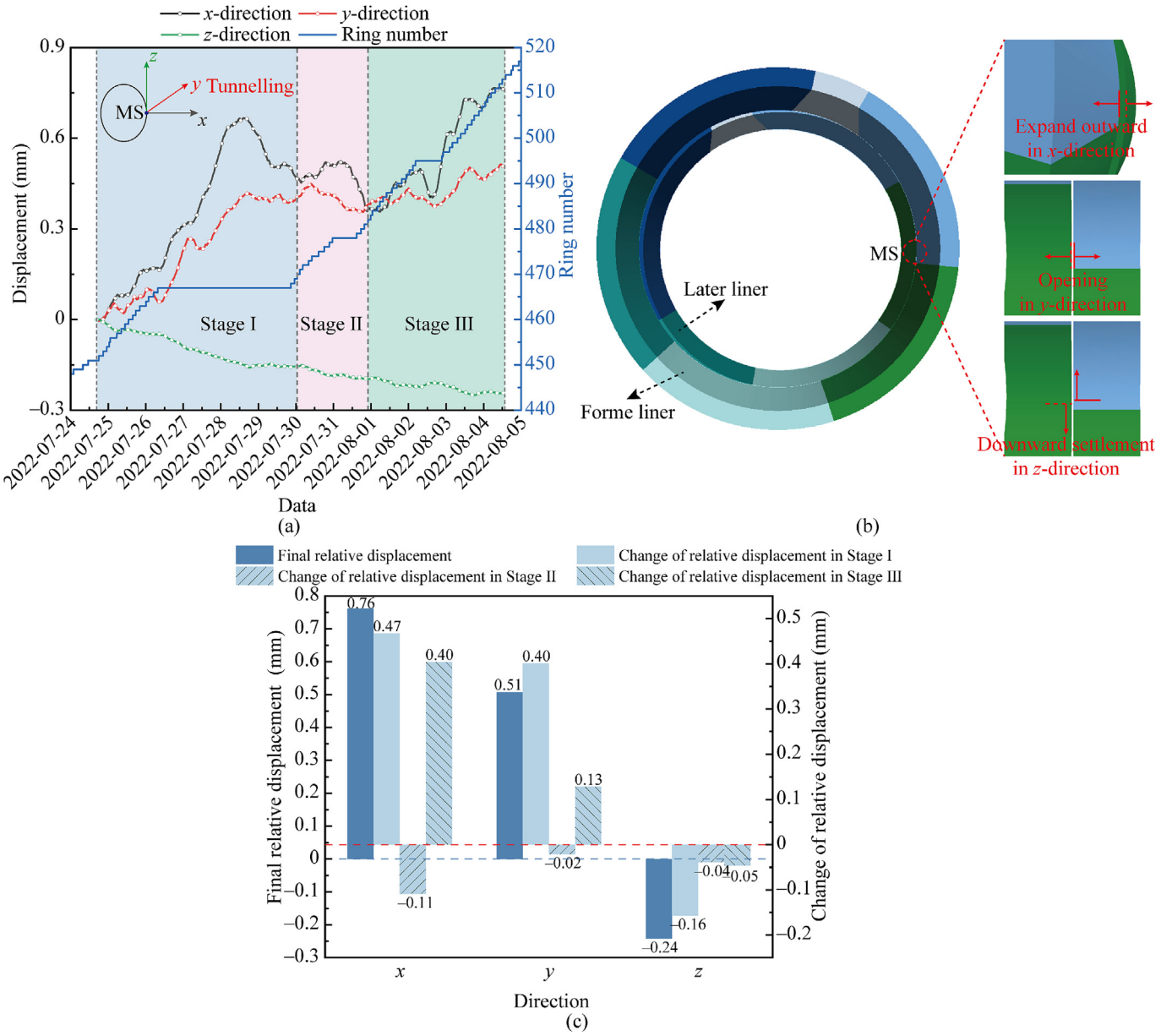

Fig. 13. Relative displacement of the segment at MS: (a) evolutionary process, (b) deformation mode, and (c) characteristic values.

The geological parameters used in the numerical simulation are summarized in Table 3.

The model (Fig. 14) integrates EPBS, segmental lining, grouting, and construction loads (face pressure, EPBS weight, grouting pressure, jack thrust, backup train pressure). The EPBS was modeled with Geogrid elements in six sections (1.5 m step width), with increasing elastic modulus from front to rear to simulate shield conicity. Segmental lining employed liner elements with staggered joints, accounting for inter-segment connections and grouting interactions. Grouting used elastic elements (Young's modulus: 20 MPa, Poisson's ratio: 0.2). Face pressure acted vertically on the tunnel face, matching horizontal ground stress at the vault and increasing linearly (11 kPa/m gradient). The EPBS weight is simulated as distributed pressure with a total force of 5580 kN. Grouting pressure at the shield tail equaled vertical ground stress at the vault, increasing linearly (11 kPa/m gradient). The jack thrust acts on the latest ring, assumed to be uniformly distributed along the circumference. Backup train pressure is simulated by vertical forces on two parallel lines (3 m apart, 88.5 m range) with a force equal to the train's weight. The twin tunnels were excavated sequentially with a 100 m lagging distance between faces, reflecting actual construction. Modeling details follow Wang et al. (2024b).

Figure 15 shows the comparison between the calculated and measured horizontal displacement of the monitoring points MR1 and MR2. Throughout the monitoring process, the calculated results align well with the measured data, especially at the MR2 monitoring point. The MR1

Table 3
Parameters used for modelling.

Parameter	ρ (kg/m^3)	E_m (MPa)	μ	σ_{ci} (MPa)	m_b	s	a	b	k (m/s)	λ
Value	2600	93.02	0.23	29.06	0.589	2.87×10^{-5}	0.613	0.12	5.79×10^{-6}	0.98

Note: ρ is the density, E_m is the Young's modulus of the rock mass, μ is Poisson's ratio, k is the permeability coefficient, and λ is the lateral pressure coefficient.

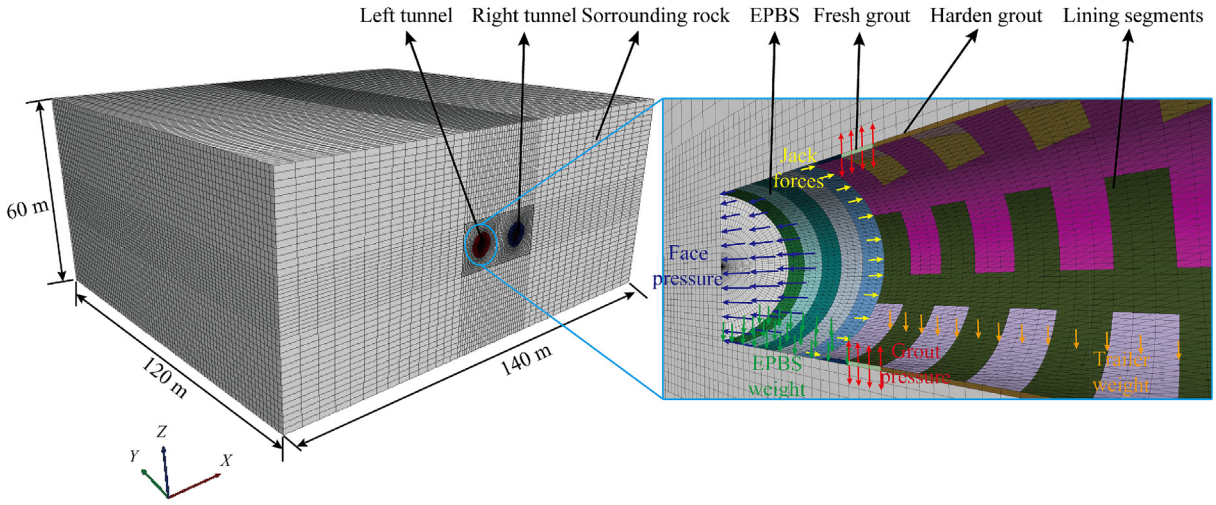

Fig. 14. 3D refined numerical model.

point is closer to the free surface of the tunnel wall, making it more susceptible to excavation-induced damage, which leads to a monitored displacement exceeding the simulated displacement.

4.2 Numerical results

4.2.1 Excess pore pressure

Figure 16(a) shows the longitudinal distribution of excess pore pressure around the tunnel caused by a single excavation step. The distribution results from the eight numerical monitoring points show that the longitudinal distribution pattern of excess pore pressure is consistent at all monitoring points. The distribution induced by EPBS construction is determined by the relative distance from the tunnel face. This phenomenon has been observed in single-tunnel cases and persists in the twin-tunnel case. The excess pore pressure distribution adequately reflects the influence of various construction stages of EPBS. The arrival of the tunnel face results in an increase in excess pore pressure, with the influence range approximately equal to one length of the shield machine (9 m). In the range where the shield machine is located, excess pore pressure decreases dramatically due to stress release from overcut. Grouting at the shield tail causes a sudden increase in excess pore pressure, while the removal of the shield tail leads to a decrease. Finally, the pressure rebounds and gradually dissipates after the shield tail void is closed. The influence of these construction steps on excess pore pressure extends about

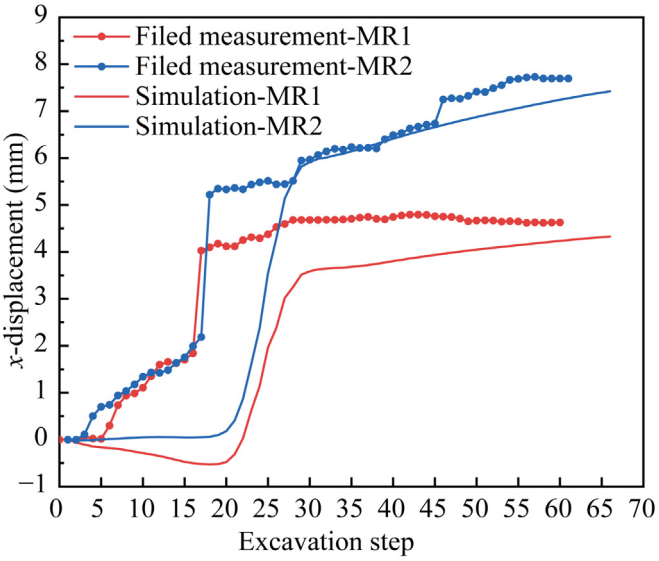

Fig. 15. Validation of numerical model.

two lengths of the shield machine. Figure 16(b) shows the distribution of excess pore pressure in front of the tunnel face due to single-step excavation. The excess pore pressure distribution in front of the tunnel face of a single tunnel can usually be fitted by Eq. (10) (Shi et al., 2021).

$$\Delta U = \Delta U_{max}[\sqrt[3]{1 + (y/R)^3} - y/R], \quad (10)$$

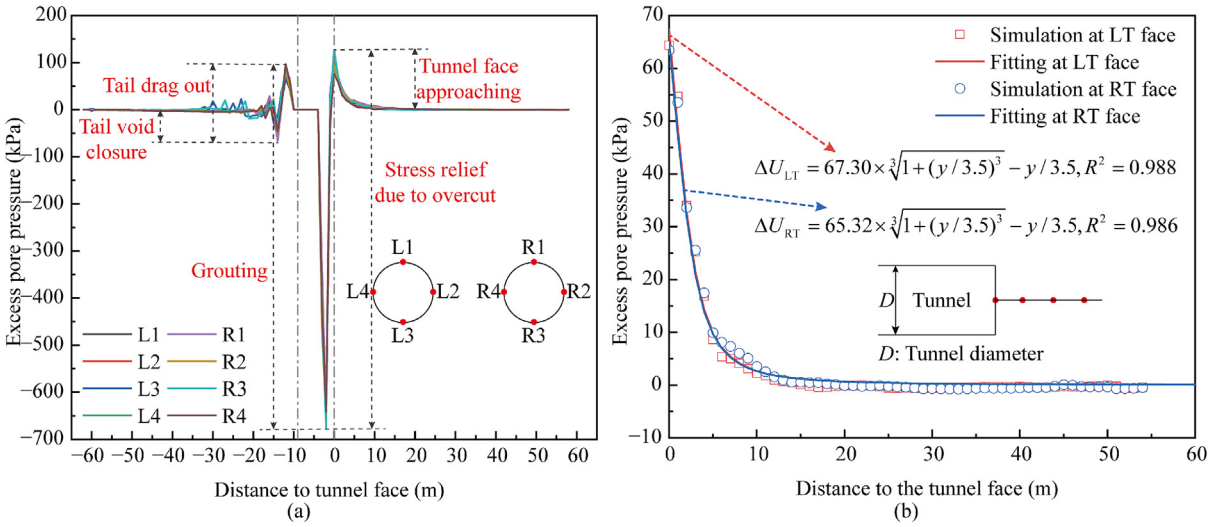

Fig. 16. Excess pore pressure: (a) around the tunnel, and (b) in front of the tunnel face.

where ΔU_{max} is the maximum excess pore pressure, y is the longitudinal distance to the tunnel face, and R is the tunnel radius. Figure 16(b) shows that the R^2 value of the fitted equation exceeds 0.95 for both the first and second tunnels, indicating that the fitted equation is applicable for excess pore pressure caused by a single excavation step in the twin tunnel.

4.2.2 Vault settlement

Figure 17(a) shows the evolution of the settlement trough at the tunnel vault in the central cross-section during the excavation of the twin tunnel. It indicates that vault settlement mainly occurs after the passage of the tunnel face. Severe stress relief from overcut and shield conicity results in significant vault settlement. During the excavation of the second tunnel, the vault settlement trough gradually moves to the right, forming a new settlement trough near the second tunnel, while the vault settlement of the first tunnel further increases. Settlement in the middle area between the twin tunnels develops slowly, forming a W-shaped settlement trough in the cross-section. Additionally, the transversal distribution of vault settlement due to twin tunnel excavation is asymmetrical, similar to observations by previous authors through field monitoring and modeling tests (Chen et al., 2011; He et al., 2012; Suwansawat & Einstein, 2007). In Fig. 17(b), the settlement trough from the second tunnel excavation is obtained by subtracting the trough formed by the first tunnel excavation from the final vault settlement trough. It shows that the vault settlement troughs from twin tunnel construction have similar shapes. However, settlements from the second tunnel construction are deeper compared to the first tunnel, similar to the experimental results of Chapman et al. (2007). Excavation of the second tunnel increased the maximum vault settlement of the existing tunnel by 0.57%, while the presence of the existing tunnel increased the maximum vault settlement above the second tunnel by 6.12% compared to the single-tunnel case. After completing the twin-tunnel excavation, the maximum vault settlement occurs directly above the second tunnel, increasing by 14.08% compared to the single-tunnel case.

4.2.3 Lining responses

Figure 18(a), (b), and (c) shows the normal displacement, normal force, and bending moment of the lining in the first tunnel during the construction of the second tunnel, respectively. The distribution pattern of the lining responses is similar after the excavation of the second tunnel. The normal displacement (positive for outward displacement) is overall in compression. During the excavation of the second tunnel, the inward displacement in the existing tunnel increases except on the right side, where inward displacement is gradually reduced due to stress release from the excavation of the second tunnel. This reflects the trend of the rock mass in the middle region of the twin tunnels moving towards the second tunnel. As the excavation progresses, the distribution pattern of normal force (positive in tension) remains basically the same, divided into six parts by the combination of segmental lining, and decreases significantly at the joints. The bending moment distribution is generally circular, with abrupt changes mainly at the segment joints. From the development of lining response extremes, as shown in Fig. 18(d), the excavation of the second tunnel increases the lining response in the existing tunnel with increased response extremes. This indicates that structural loads shift during the second tunnel excavation, causing the lining structure in the existing tunnel to bear larger normal force and bending moment. When the tunnel face of the second tunnel is 6.4D away from the monitoring ring, the lining response in the existing tunnel stabilizes. The final lining responses in the second tunnel are similar to those in the single-tunnel case, indicating that the second tunnel is not significantly affected by the existing tunnel in terms of lining response,

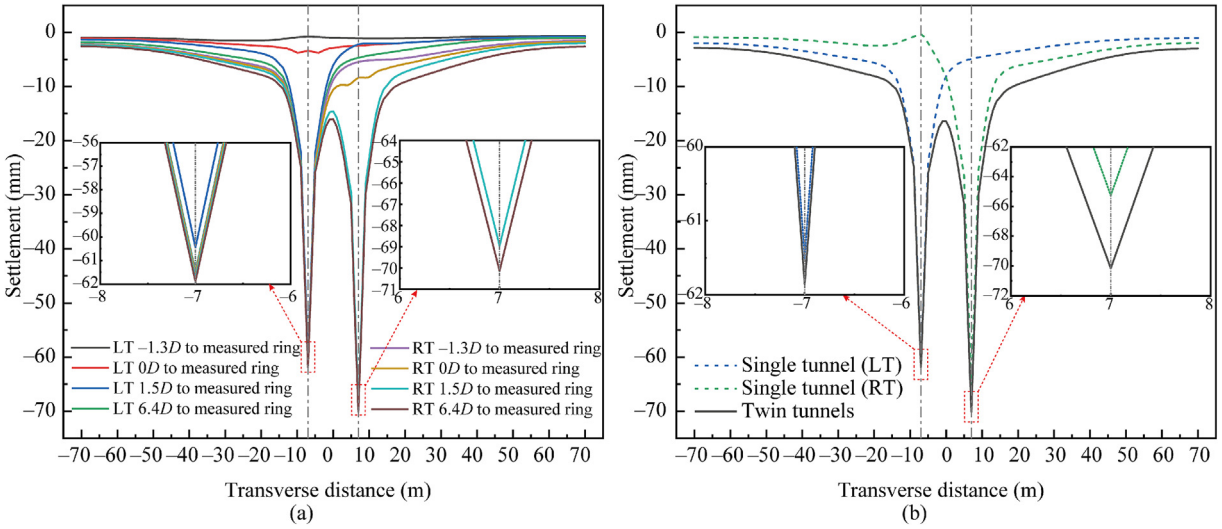

Fig. 17. Vault settlement: (a) evolutionary process, and (b) comparison of twin tunnels.

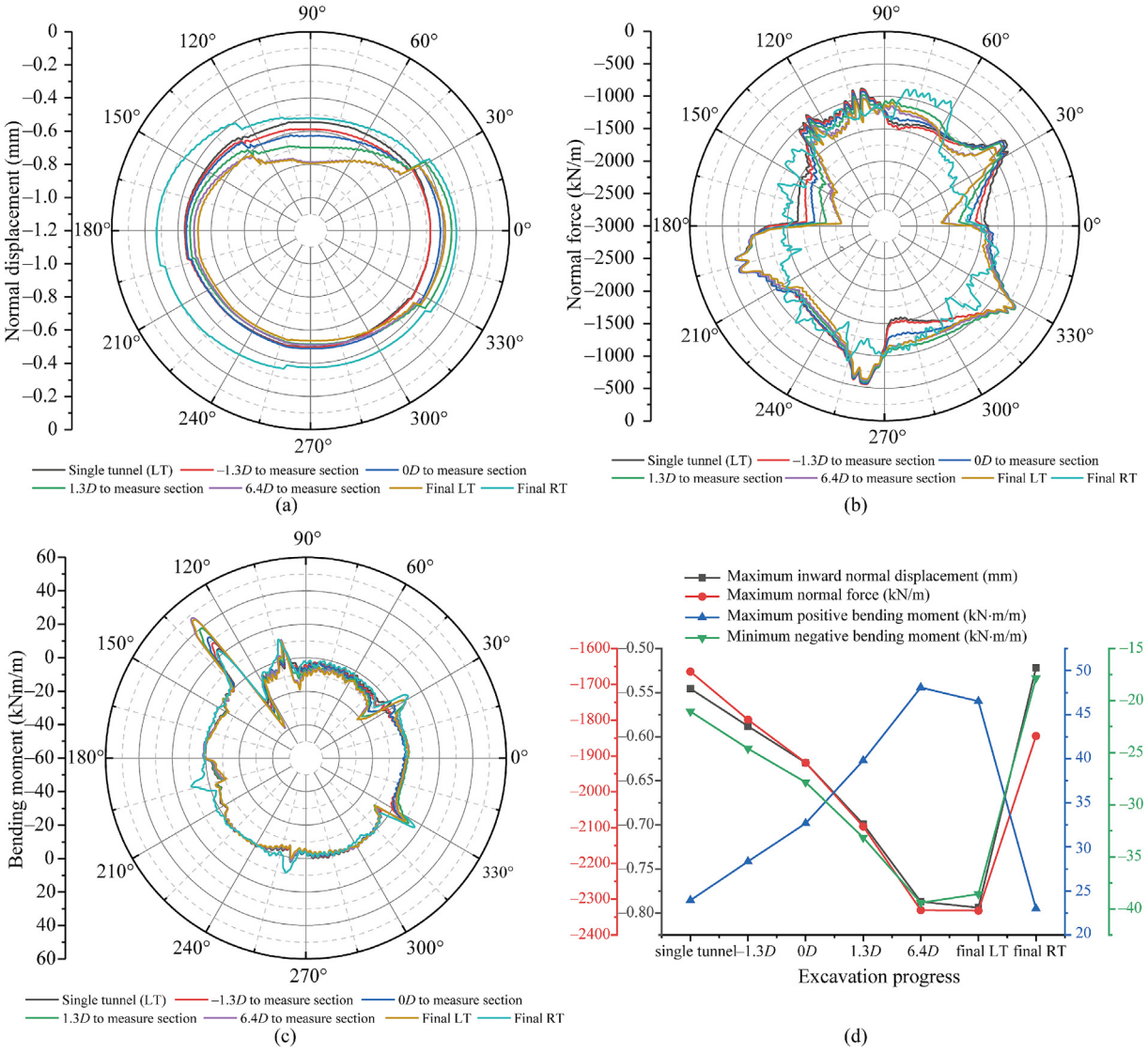

Fig. 18. Evolution process of lining response: (a) normal displacement, (b) normal force, (c) bending moment, and (d) lining response extremes.

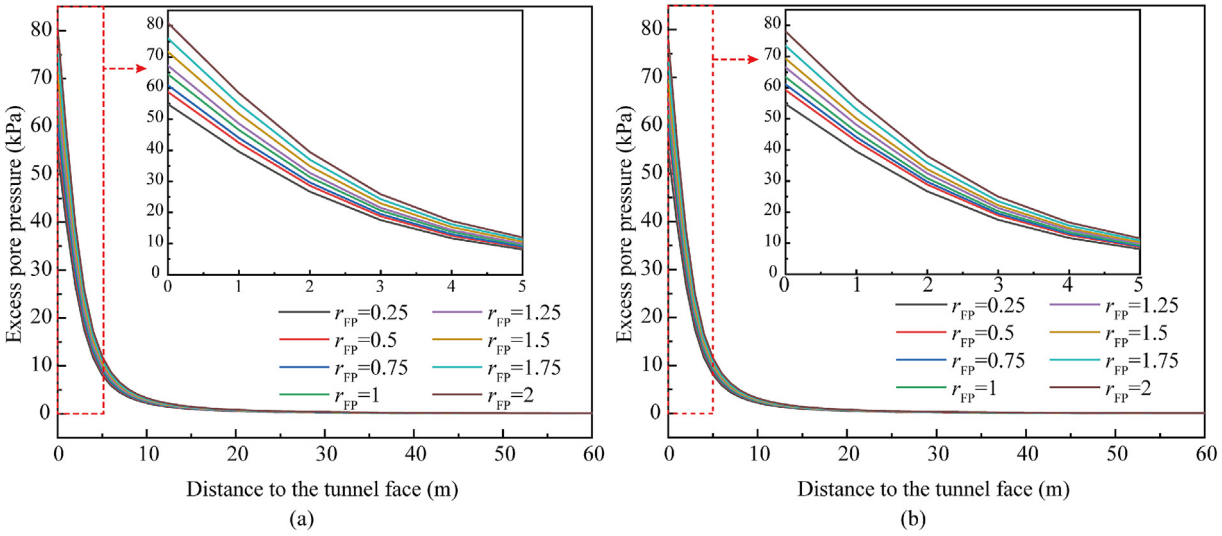

Fig. 19. Effect of face pressure on excess pore pressure: (a) the first tunnel, and (b) the second tunnel.

and the excavation process is similar to that in the single-tunnel case.

4.3 Effects of face pressure

To study the effect of face pressure on the hydraulic-rock-structural response of the twin tunnel, eight face pressure ratios (r_{FP}) were set, defined as the ratio of the face pressure at the vault to the horizontal ground stress: 0.25, 0.5, 0.75, 1, 1.25, 1.5, 1.75, and 2. As shown in Fig. 19, increasing face pressure does not change the distribution pattern of excess pore pressure in front of the tunnel face, but it increases the maximum excess pore pressure. This increase is almost linear and applies to both the first tunnel and the second tunnel.

As for the vault settlement, as shown in Fig. 20, increased face pressure can effectively resist vault settlement in front of the tunnel face and even change the form of the settlement trough, which applies to both the first and second tunnels. Moreover, the tendency of vault settlement in front of the tunnel face is effectively halted at $r_{FP} > 0.75$. However, during the excavation of the second tunnel, increased face pressure did not significantly affect the vault settlement of the existing tunnel.

For the lining response, as shown in Fig. 21, face pressure in the second tunnel has no effect on the distribution pattern of lining responses. The main effect is an increase in the inward normal displacement on the right side of the lining in the existing tunnel with increased face pressure. Figure 21(d) shows that increased face pressure in the second tunnel leads to an increase in maximum inward normal displacement and maximum normal force, as well as a decrease in the bending moment in the existing tunnel. This indicates that larger face pressure causes partial transfer of structural loads, with the lining in the existing tunnel bearing a larger normal force and smaller bending moment, resulting in greater normal displacement. Overall, setting the r_{FP} between 0.75 and 1 is reasonable for stabilizing the supporting tunnel face and reducing the comprehensive disturbance effect during construction, which aligns with the recommendation of Do et al. (2021).

4.4 Effects of grouting pressure

To study the effect of grouting pressure on the hydraulic-rock-structural response of the twin tunnel, eight grouting pressure ratios (r_{GP}), defined as the ratio of the grouting pressure to the vertical ground stress at the vault, were set at 0.25, 0.5, 0.75, 1, 1.25, 1.5, 1.75, and 2. As shown in Fig. 22, grouting pressure does not influence the distribution pattern or the magnitude of the excess pore pressure in front of the tunnel face but mainly affects the grouting ring. Increasing grouting pressure results in higher excess pore pressure in the grouting ring, affecting both the first and second tunnels equally, though the increase is more significant in the second tunnel.

Regarding vault settlement, as shown in Fig. 23, grouting pressure does not affect the morphology of the vault settlement troughs in either single or twin tunnel cases. However, increasing grouting pressure can significantly reduce the maximum vault settlement. This reduction is most significant in single-tunnel cases with r_{GP} between 1.25 and 1.5, and in twin-tunnel cases with r_{GP} between 1.75 and 2.

For the lining response, as shown in Fig. 24, grouting pressure in the second tunnel does not affect the distribution pattern of the lining response in the existing tunnel. Figure 24(d) shows that increasing grouting pressure in the second tunnel causes the maximum inward normal displacement and maximum normal force in the existing tunnel to first decrease and then increase, with a turning point at r_{GP} from 0.75 to 1. Additionally, increasing grouting pressure leads to an overall increase in the bending moment, especially the maximum positive bending

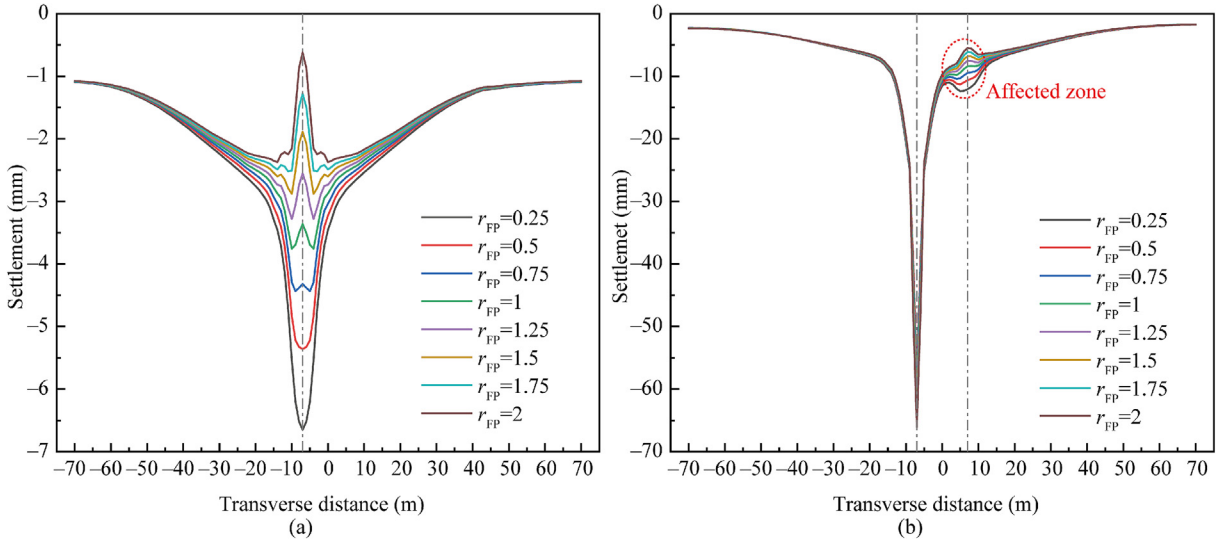

Fig. 20. Effect of face pressure on vault settlement: (a) the first tunnel, and (b) the second tunnel.

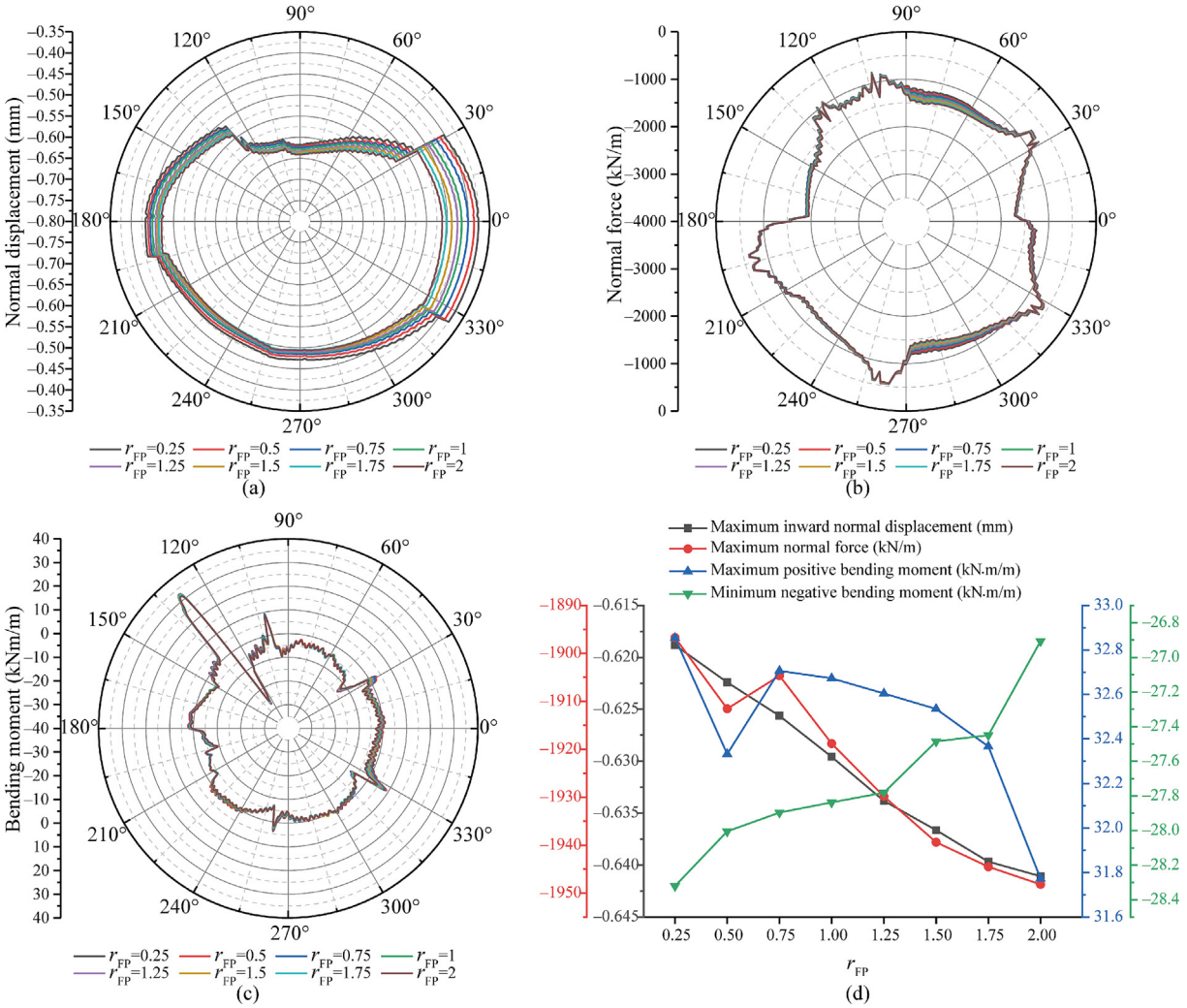

Fig. 21. Effect of face pressure on lining response: (a) normal displacement, (b) normal force, (c) bending moment, and (d) lining response extremes.

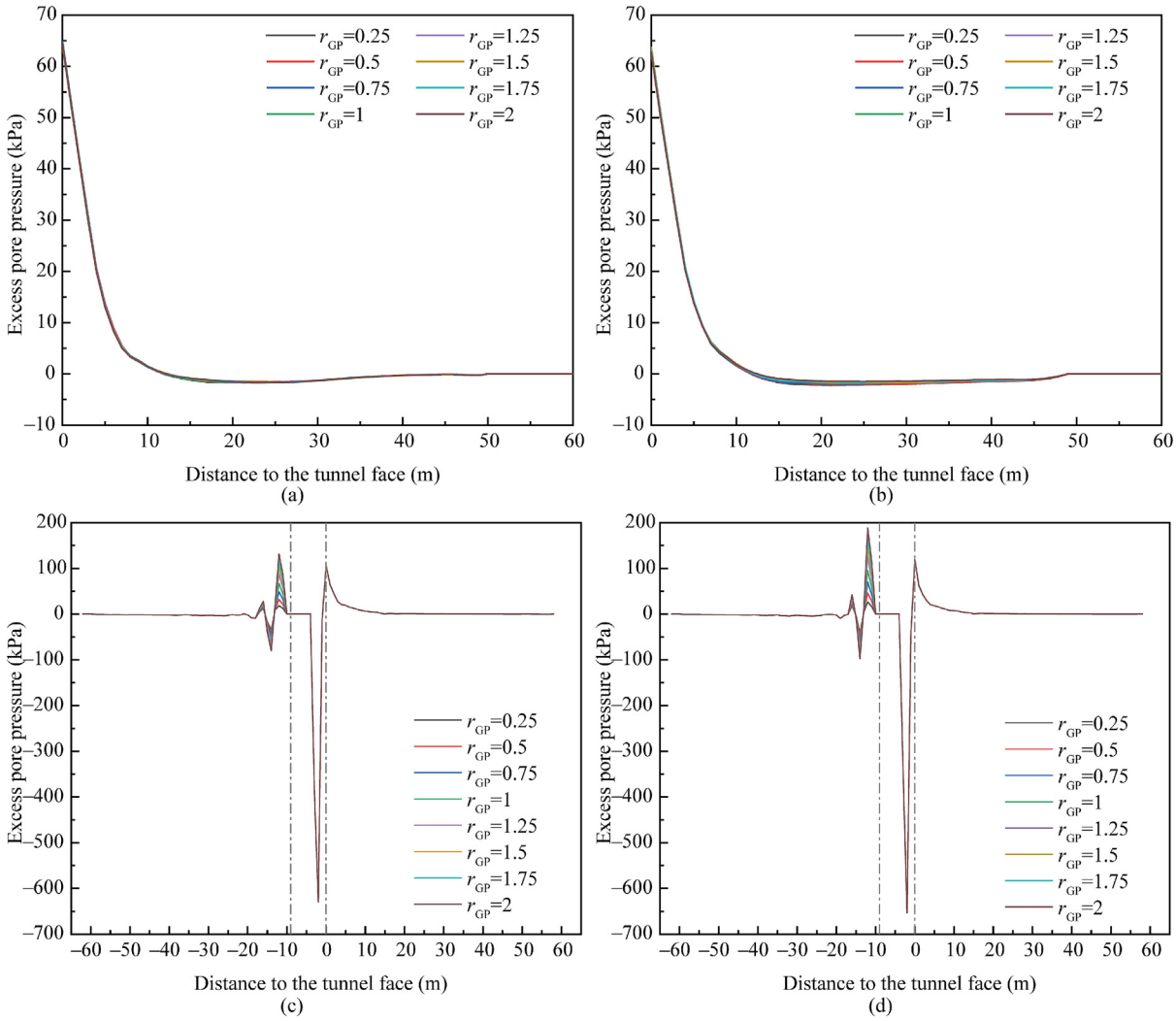

Fig. 22. Effect of grouting pressure on excess pore pressure: (a) in front of the first tunnel face, (b) in front of the second tunnel face, (c) at the vault of the first tunnel, and (d) at the vault of the second tunnel.

moment, which increases sharply and linearly at $r_{GP} \geq 1$. Overall, setting the r_{GP} to 1 is reasonable for supporting the stress of the surrounding rock of the tunnel vault and reducing the construction disturbance, which aligns with the recommendation of Do et al. (2021).

5 Conclusions

In this paper, an advanced MEMS multi-sensor fusion automated monitoring system (MFAS-TunRS) is developed for real-time, multi-parameter monitoring of the hydraulic-rock-structural response in shield tunnels. A refined 3D numerical model analyzed the evolution of pore pressure, vault settlement, and lining response, as well as the impact of construction parameters. The following main conclusions are drawn:

(1) The pore pressure evolved through three stages: a sudden drop and stabilization before the shield's arrival, during its passage, and afterward. This behavior is tied to excavation activity and the shield's lower earth chamber pressure. Final pore pressure increased with distance from the second tunnel, whereas dissipation rates decreased.

(2) The earth pressure evolution differed between far/near ends but exhibited three-stage behavior. Far-end earth pressure surged rapidly before the shield's arrival, rose slowly during passage, and then stabilized afterward. At the near end, stress at MR1 resembles the far end, while MR2 decreases rapidly during passage, then quickly recovers and stabilizes. The final earth pressure distribution is positively correlated with distance from the second tunnel.

(3) The rock displacement in x- and z-directions follows three stages: rapid growth, slowed progression, and stabilization, while y-direction displacement remained minimal. Displacement magnitude and components are negatively correlated with distance from the second tunnel. Primary displacement occurred pre-shield arrival, followed by secondary

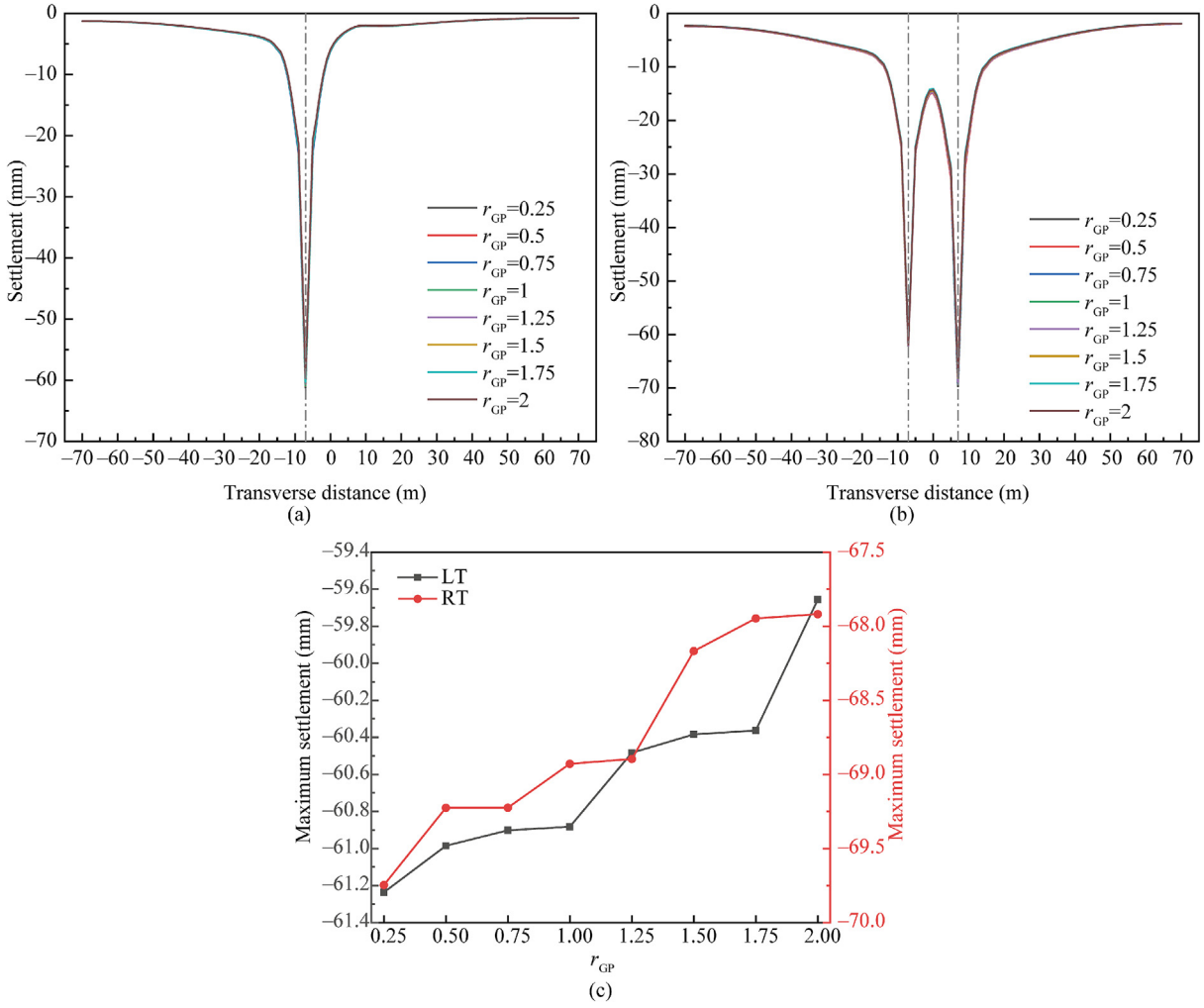

Fig. 23. Effect of grouting pressure on vault settlement: (a) the first tunnel, (b) the second tunnel, and (c) maximum vault settlement.

effects from grout hardening and pore pressure/rock stress equilibration post-passage. Minimal displacement occurred during shield passage near adjacent tunnels.

(4) Lining and surrounding rock responses exhibited similar trends, with additional stress evolving in three stages: rapid increase, stabilization after a sudden rise, and stabilization after a rapid drop. Relative displacement shows a rapid increase, a slight decrease, a slow increase, and stabilization. Circumferential additional stress changes exceeded longitudinal ones. Relative displacement ranked $x > y > z$, confirming lateral unloading from second-tunnel excavation as the dominant perturbation source for existing tunnel linings.

(5) Based on refined 3D numerical simulations, the hydraulic-rock-structural response to twin tunnel construction is closely tied to the process. Excess pore pressure distribution is primarily influenced by the shield cut location. The longitudinal excess pore pressure distribution follows five stages: rise from tunnel face arrival, fall from overcut, rise from grouting, fall from trailing, and equilibrium restoration behind the shield tail. Twin tunnel excavation induced greater vault settlement, forming a W-shaped settlement trough. It also caused greater unloading, increasing deformation and structural force on the existing tunnel lining. The second tunnel's lining response was nearly unaffected by the existing tunnel, resembling a single-tunnel case.

(6) The impact of face and grouting pressure is confined to the tunnel face front and grouting ring. Higher face and grouting pressures effectively reduce vault settlement but increase excess pore pressure and lining response. Applying r_{FP} (from 0.75 to 1) and r_{GP} = 1 proved optimal for stabilizing the tunnel face while minimizing overall disturbances.

In addition, the MEMS monitoring system presented in this study offers further potential for advancement, for instance, by replacing the unidirectional stress sensor with a triaxial stress sensor to enable comprehensive monitoring and analysis of earth pressure. Moreover, the MEMS monitoring system is not limited to tunnel engineering but can

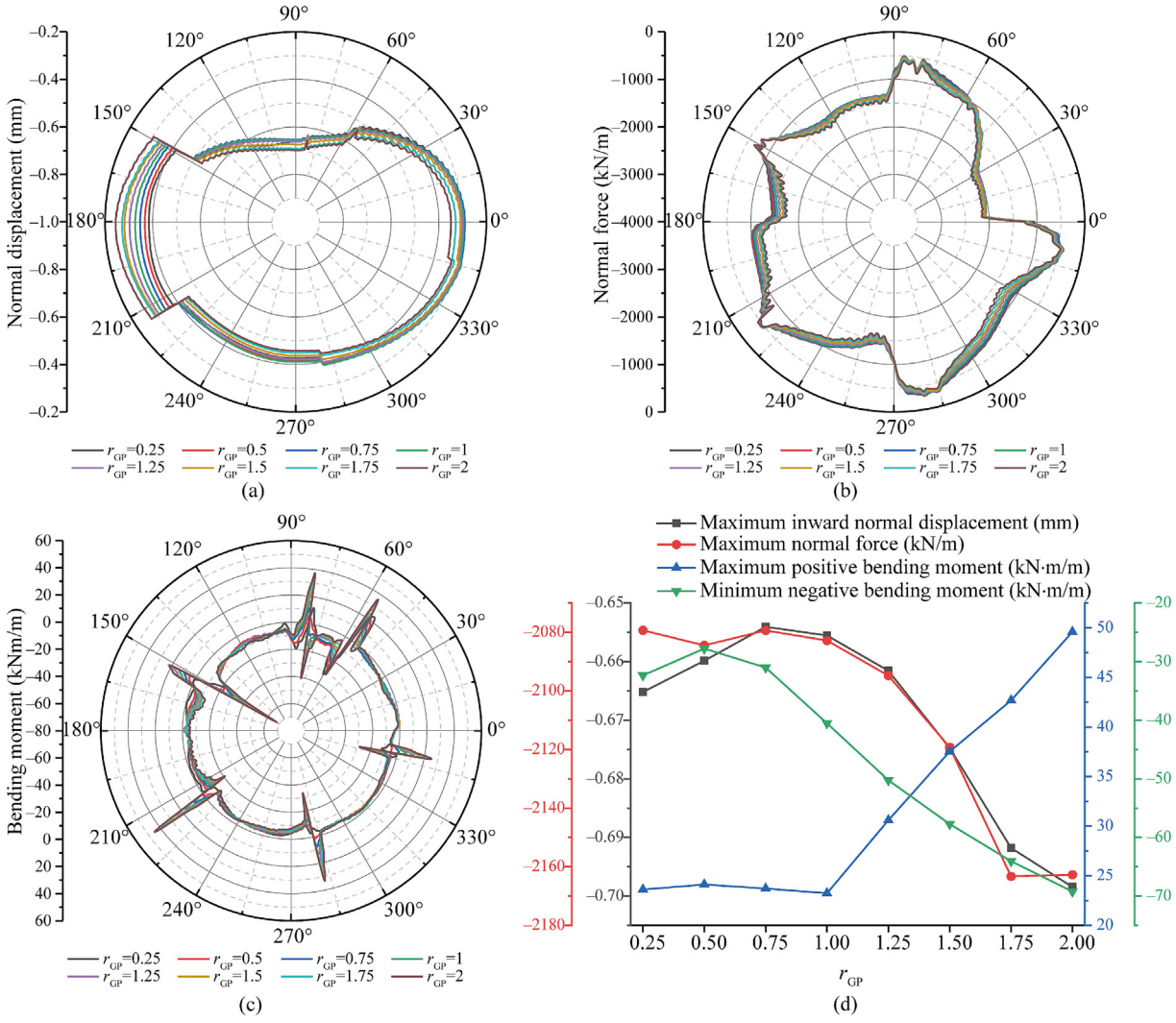

Fig. 24. Effect of grouting pressure on lining response: (a) normal displacement, (b) normal force, (c) bending moment, and (d) lining response extremes.

be adapted for other geotechnical applications, including deep excavation and slope engineering, offering flexibility for various projects.

Data availability

The data that support the findings of this study are available from the corresponding author upon reasonable request.

CRediT authorship contribution statement

Chengwen Wang: Writing – original draft, Investigation, Data curation, Formal analysis, Software, Conceptualization. **Xiaoli Liu:** Supervision, Funding acquisition, Writing – review & editing, Project administration. **Nan Hu:** Formal analysis, Writing – review & editing. **Wenli Yao:** Writing – review & editing, Formal analysis. **Enzhi Wang:** Writing – review & editing, Supervision, Funding acquisition. **Jianhong Jia:** Project administration, Investigation.

Declaration of competing interest

The authors declare that they have no known competing financial interests or personal relationships that could have appeared to influence the work reported in this paper.

Acknowledgement

This work was supported by the National Key Research and Development Program of China (Grant No. 2023YFB4005500), the National Natural Science Foundation of China (Grant Nos. 52090081 and 52079068), and the State Key Laboratory of Hydroscience and Hydraulic Engineering, China (Grant No. 2021-KY-04).

References

Allahverdi, N., Bakhshi, M., Partovi, M., & Nasri, V. (2023). 3D-nonlinear finite element analysis of staged shield-driven tunnel excavation with a focus on response of segmental tunnel lining. *Geomechanics and Tunnelling, 16*(1), 60–67.

Almheiri, Z., Meguid, M., & Zayed, T. (2021). Failure modeling of water distribution pipelines using meta-learning algorithms. *Water Research, 205*, 117680.
Awaga, M. A., Moaaz, A. O., & Ghazaly, N. M. (2024). Numerical analysis of dual-fuel diesel engines in compression ignition engines: A review. *Babylonian Journal of Mechanical Engineering, 2024*, 49–63.
Barla, M., & Insana, A. (2023). Energy tunnels as an opportunity for sustainable development of urban areas. *Tunnelling and Underground Space Technology, 132*, 104902.
Bezuijen, A., Pruiksma, J. P., & van Meerten, H. H. (2001). Pore pressures in front of tunnel, measurements, calculations and consequences for stability of tunnel face. *Modern Tunneling Science And T*. CRC Press.
Chapman, D. N., Ahn, S. K., & Hunt, D. V. (2007). Investigating ground movements caused by the construction of multiple tunnels in soft ground using laboratory model tests. *Canadian Geotechnical Journal, 44*(6), 631–643.
Chen, J.-F., Kang, C.-Y., & Shi, Z.-M. (2015). Displacement monitoring of parallel closely spaced highway shield tunnels in marine clay. *Marine Georesources & Geotechnology, 33*(1), 45–50.
Chen, R. P., Zhu, J., Liu, W., & Tang, X. W. (2011). Ground movement induced by parallel EPB tunnels in silty soils. *Tunnelling and Underground Space Technology, 26*(1), 163–171.
Chen, R.-P., Lin, X.-T., Kang, X., Zhong, Z.-Q., Liu, Y., Zhang, P., & Wu, H.-N. (2018). Deformation and stress characteristics of existing twin tunnels induced by close-distance EPBS under-crossing. *Tunnelling and Underground Space Technology, 82*, 468–481.
Cheng, C., Zhao, W., Qi, D., Han, J., Jia, P., Chen, Y., & Bai, Q. (2019). A case study on the stability of the shield excavation face in full-section coarse sand. *Sustainable Cities and Society, 47*, 101486.
Chortis, F., & Kavvadas, M. (2021). Three-dimensional numerical investigation of the interaction between twin tunnels. *Geotechnical and Geological Engineering, 39*(8), 5559–5585.
Clayton, C. R. I., Van Der Berg, J. P., & Thomas, A. H. (2006). Monitoring and displacements at Heathrow Express Terminal 4 station tunnels. *Géotechnique, 56*(5), 323–334.
Cui, L., Yang, W., Zheng, J., & Sheng, Q. (2023). Improved equations of ground pressure for shallow large-diameter shield tunnel considering multiple impact factors. *Tunnelling and Underground Space Technology, 138*, 105166.
Do, N. A., Dias, D., & Oreste, P. (2015). 3D numerical investigation on the interaction between mechanized twin tunnels in soft ground. *Environmental Earth Sciences, 73*(5), 2101–2113.
Do, N. A., Dias, D., Vu, T. T., & Dang, V. K. (2021). Impact of the shield machine's performance parameters on the tunnel lining behaviour and settlements. *Environmental Earth Sciences, 80*(16), 507.
Gao, S. M., Chen, J. P., Zuo, C. Q., & Wang, W. (2017). Monitoring of three-dimensional additional stress and strain in shield segments of former tunnels in the construction of closely-spaced twin tunnels. *Geotechnical and Geological Engineering, 35*(1), 69–81.
Gu, G., Zhang, Z., Huang, X., Li, Y., & Lei, Q. (2024). A finite element-based dynamic simulation method for modeling shield-ground interactions: 3D numerical simulations with comparison to physical experiments. *Computers and Geotechnics, 169*, 106262.
Guo, D., Zhu, X., Xie, J., Zhang, C., Zhao, Z., & Zheng, L. (2021). Undergraduate program for urban underground space engineering in China: Exploration and practice. *Tunnelling and Underground Space Technology, 116*, 104084.
Han, L., Ye, G., Chen, J., Xia, X., & Wang, J. (2017). Pressures on the lining of a large shield tunnel with a small overburden: A case study. *Tunnelling and Underground Space Technology, 64*, 1–9.
He, C., Feng, K., Fang, Y., & Jiang, Y. (2012). Surface settlement caused by twin-parallel shield tunnelling in sandy cobble strata. *Journal of Zhejiang University SCIENCE A, 13*(11), 858–869.
Islam, M. S., & Iskander, M. (2021). Twin tunnelling induced ground settlements: A review. *Tunnelling and Underground Space Technology, 110*, 103614.
Jia, R., Zheng, G., & Jiang, Y. (2024). The effect of clay structure formed during deposition on the ground deformation induced by shield tunneling. *Tunnelling and Underground Space Technology, 147*, 105689.
Jiang, J., Gan, W., Hu, Y., Li, S., Deng, J., Yue, L., Yang, Y., Nan, Q., Pan, J., Liu, F., & Wang, H. (2021). Real-time monitoring method for unauthorized working activities above the subway tunnel based on ultra-weak fiber Bragg grating vibration sensing array. *Measurement, 182*, 109744.
Lambrughi, A., Medina Rodríguez, L., & Castellanza, R. (2012). Development and validation of a 3D numerical model for TBM–EPB mechanised excavations. *Computers and Geotechnics, 40*, 97–113.
Li, P., Wang, Q., Li, J., Pei, Y., & He, P. (2024). Mechanism and impact of water seepage during shield tunnelling in sandy cobble strata: A case study. *Tunnelling and Underground Space Technology, 149*, 105784.
Liu, Y., Liao, S., Chen, L., & Liu, M. (2022). Structural responses of DOT tunnel induced by shield under-crossing in close proximity in soft ground. Part I: Field measurement. *Tunnelling and Underground Space Technology, 128*, 104623.
Rauch, F., & Fischer, O. (2024). Structural behavior of segmental tunnel linings based on in situ measurements. *Journal of Performance of Constructed Facilities, 38*(4), 04024014.
Shi, J., Wang, F., Zhang, D., & Huang, H. (2021). Refined 3D modelling of spatial-temporal distribution of excess pore water pressure induced by large diameter slurry shield tunneling. *Computers and Geotechnics, 137*, 104312.
Suwansawat, S., & Einstein, H. H. (2007). Describing settlement troughs over twin tunnels using a superposition technique. *Journal of Geotechnical and Geoenvironmental Engineering, 133*(4), 445–468.
Wan, M. S. P., Standing, J. R., Potts, D. M., & Burland, J. B. (2019). Pore water pressure and total horizontal stress response to EPBM tunnelling in London Clay. *Géotechnique, 69*(5), 434–457.
Wang, C., Liu, X., Song, D., Wang, E., He, Z., & Tan, R. (2024a). Structural response of former tunnel in the construction of closely-spaced cross-river twin tunnels. *Tunnelling and Underground Space Technology, 147*, 105652.
Wang, C., Liu, X., Song, D., Wang, E., Yan, G., & Zhou, R. (2024b). Three-dimensional hydro-mechanical coupling numerical simulation of shield-driven cross-river twin tunnels: A case study. *Underground Space, 16*, 106–125.
Wang, C., Liu, X., Song, D., Wang, E., & Zhang, J. (2023). Elasto-plastic analysis of the surrounding rock mass in circular tunnel using a new numerical model based on generalized nonlinear unified strength theory. *Computers and Geotechnics, 154*, 105163.
Wang, Z., Yao, W., Cai, Y., Xu, B., Fu, Y., & Wei, G. (2019). Analysis of ground surface settlement induced by the construction of a large-diameter shallow-buried twin-tunnel in soft ground. *Tunnelling and Underground Space Technology, 83*, 520–532.
Wu, H.-N., Xu, X.-P., Chen, R.-P., Liu, Y., Cheng, H.-Z., & Xiao, C. (2024a). Observed uplift behaviors of segmental lining during shield tunneling in hard rock: A case study from Changsha, China. *Tunnelling and Underground Space Technology, 150*, 105816.
Wu, S., Hu, X., Fu, W., & Li, K. (2024b). Evaluation of segmental lining response during shield tunnel construction based on field measurements and 3D FEM simulation. *Transportation Geotechnics, 44*, 101135.
Xie, H., Zhang, Y., Chen, Y., Peng, Q., Liao, Z., & Zhu, J. (2021). A case study of development and utilization of urban underground space in shenzhen and the guangdong-hong kong-macao greater bay area. *Tunnelling and Underground Space Technology, 107*, 103651.
Yin, M., Jiang, H., Jiang, Y., Sun, Z., & Wu, Q. (2018). Effect of the excavation clearance of an under-crossing shield tunnel on existing shield tunnels. *Tunnelling and Underground Space Technology, 78*, 245–258.
Zhang, Y., Xie, X., Li, H., Zhou, B., Wang, Q., & Shahrour, I. (2022). Subway tunnel damage detection based on in-service train dynamic response, variational mode decomposition, convolutional neural networks and long short-term memory. *Automation in Construction, 139*, 104293.
Zheng, G., Sun, J., Zhang, T., Zhang, X., Li, X., Cheng, H., Bai, N., & Diao, Y. (2023). Numerical study on the impact of local failure on adjacent structures in a shield tunnel. *Acta Geotechnica, 18*(4), 2155–2168.
Zheng, H., Li, P., & Ma, G. (2021). Stability analysis of the middle soil pillar for asymmetric parallel tunnels by using model testing and numerical simulations. *Tunnelling and Underground Space Technology, 108*, 103686.
Zhou, H., Gao, Y., Zhang, C., Yang, F., Hu, M., Liu, H., & Jiang, Y. (2018). A 3D model of coupled hydro-mechanical simulation of double shield TBM excavation. *Tunnelling and Underground Space Technology, 71*, 1–14.